Journal of Materials Chemistry A

REVIEW

View Article Online
View Journal | View Issue

Cite this: J. Mater. Chem. A, 2021, 9, 3703

Recent progress in the development of biomass-derived nitrogen-doped porous carbon

Babasaheb M. Matsagar, *[a] Ren-Xuan Yang, [a] Saikat Dutta, [b] Yong Sik Ok [c] and Kevin C.-W. Wu *[ade]

This review offers a focused discussion on the recent progress of biomass-derived nitrogen-doped porous carbon (NPC) and its applications. Various synthesis methods for biomass-derived NPCs are introduced and critically reviewed. N-doping is a promising approach for further improving the physicochemical/electrochemical properties of carbon materials. Besides, NPC synthesis from inexpensive biomass for energy storage applications is a green and sustainable strategy. NPCs can be synthesized directly from algae, chitosan, and glucosamine without using any additional N precursor. The effect of synthesis methods on the physicochemical properties of NPCs offers a direction for optimizing the properties of NPCs for diverse applications. The utilization of NPCs in various applications, including catalysis and electrochemical energy storage (*e.g.*, fuel cells, batteries, and supercapacitors), is reviewed. Besides, a discussion on the use of NPCs in oxidation and hydrogenation reactions, CO_2 capture and reduction is provided. The factors controlling the electrocatalytic performance of NPC are evaluated, such as the effect of N-content and the type of N species in NPCs. Finally, to improve the rational design of biomass-derived NPCs for catalysis and energy storage applications, an outlook and conclusion are provided.

Received 5th October 2020
Accepted 12th December 2020

DOI: 10.1039/d0ta09706c

rsc.li/materials-a

[a]Department of Chemical Engineering, National Taiwan University, No. 1, Sec. 4, Roosevelt Road, Taipei 10617, Taiwan. E-mail: matsagar03@ntu.edu.tw; kevinwu@ntu.edu.tw

[b]Biological & Molecular Science Laboratory, Amity Institute of Click Chemistry Research & Studies, Amity University, Sector 125, Noida, India

[c]Korea Biochar Research Center, APRU Sustainable Waste Management & Division of Environmental Science and Ecological Engineering, Korea University, Seoul, Korea

[d]Center of Atomic Initiative for New Materials (AI-MAT), NTU, Taiwan

[e]International Graduate Program of Molecular Science and Technology, National Taiwan University (NTU-MST), Taiwan

Babasaheb M. Matsagar received his Ph.D. from CSIR-National Chemical Laboratory (NCL), India, in 2016. Most of his research work was focused on developing sustainable biomass conversion methods for chemical production and energy applications using acidic ionic liquids and heterogeneous catalysts. Presently he is working as a postdoctoral researcher in the department of chemical engineering, National Taiwan University (NTU), Taiwan. His current research focused on the applications of metal-organic frameworks (MOFs) and MOF-derived materials for catalysis.

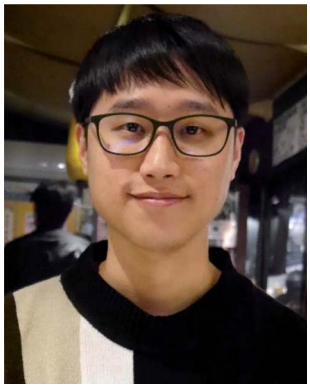

Ren-Xuan Yang received his B.S. and Ph.D. in Environmental Engineering from the National Chung Hsing University (NCHU). His Ph.D. research work focused on developing a two-stage fluidized catalyst reactor system that simultaneously treats waste plastics and produces hydrogen and carbon nanotubes (CNTs) via waste plastics gasification. He is now a postdoctoral researcher in the Department of Plastics Engineering at the University of Massachusetts Lowell. Inspired by his postdoctoral training under the guidance of Prof. Kevin C.-W. Wu at National Taiwan University (NTU), his ongoing work focuses on the synthesis of metal-organic frameworks derived materials for energy and environmental application.

1. Introduction

Biomass is an excellent alternative to fossil feedstocks to synthesize a wide variety of value-added chemicals and carbon materials such as porous carbons,[1] hierarchical porous carbons (HPCs), carbon quantum dots,[2] heteroatom-doped porous carbons, and carbon fibers.[3–7] Lignocellulosic biomass is mainly composed of lignin, cellulose, and hemicellulose.[8–10] Chitin is the second most abundant natural biopolymer made up of *N*-acetyl glucosamine derived from exoskeletons of arthropods, crustaceans, and cell walls of fungi and insects.[11] Chitosan is produced from chitin by the deacetylation of chitin. Biomass is a renewable and abundantly available source of carbon. These benefits of biomass make it an outstanding candidate for synthesizing various porous carbons and nitrogen-doped porous carbons (NPCs). Many methods are available to synthesize porous carbons from non-renewable fossil feedstock sources, which requires harsh reaction conditions.[12–14] However, these methods are not economically viable. Besides, they are environmentally unfriendly. Hence, developing a cost-efficient, sustainable process for synthesizing various functional carbons from biomass has always been a crucial topic of research.

Agricultural wastes (rice husk, bagasse, wheat straw, and cotton stalk) are significant sources of lignocellulosic biomass. The efficient utilization of raw biomass to synthesize porous carbons can lower air pollution arising from the burning of agricultural crop wastes. Besides, due to the presence of N and carbon elements in shrimp shells, algae, soybean residue, and chitosan, they are used extensively to synthesize NPCs. Mainly pyrolysis, hydrothermal carbonization (HTC), and activation methods are used for the conversion of biomass into porous carbons. Porous carbons are inexpensive and chemically stable, and have a superior electrical conductivity, and impressive Brunauer–Emmett–Teller (BET) specific surface area (500–3000 $m^2\ g^{-1}$).[15–17] However, porous carbons with a lower graphitization degree have poor electrical conductivity.

The modification of carbons by heteroatom doping not only provides acid/base characteristics but can also influence the electrical conductivity. The introduction of heteroatoms (N, O, P, and B) into the carbon framework significantly affects the capacitive performance in both organic and aqueous electrolytes. Furthermore, the heteroatoms can alter the crystalline and electronic structure of carbon by enhancing the electrical conductivity, chemical stability, and electron donating properties, leading to pseudocapacitive reactions.[18,19] The porous

Saikat Dutta has been an associate professor at the Amity Institute of Click-Chemistry Research & Studies (AICCRS) in Amity University. He is a recipient of the Ramalingaswami Fellowship and Ramanujan Fellowship from the Ministry of Science and Technology, Government of India. His past several years of research were centered on the chemistry of lignocellulose and lignocellulose-derived materials. His current research focused on the functional and biofunctional materials for therapeutic and electrochemical charge-storage applications.

Yong Sik Ok is Director of APRU Sustainable Waste Management Program and Korea Biochar Research Center at Korea University, Seoul, Korea. In 2019, Yong Sik Ok was the first South Korean to be selected as a highly cited researcher (HCR) in the field of environment and ecology by the Web of Science's HCR index with 85 highly cited papers and hot papers. He is working at the vanguard of global efforts to develop sustainable waste management strategies and technologies to address the rising crisis in electronic and plastic waste and pollution of soil and air with particulate matter. Ok has served in several positions worldwide, including as an honorary professor at the University of Queensland (Australia), visiting professor at Tsinghua University (China), adjunct professor at the University of Wuppertal (Germany), and guest professor at Ghent University (Belgium). Ok did his BS, MS and Ph.D. at Korea University in Seoul.

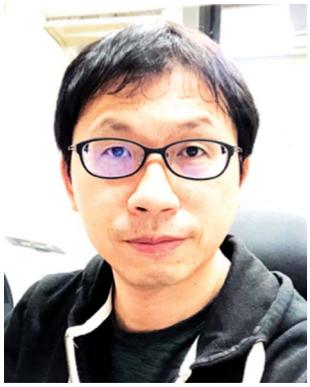

Kevin C.-W. Wu obtained his Ph.D. in 2005 from The University of Tokyo and then worked as a postdoctoral researcher at Waseda University (Japan) and Iowa State University (USA) before starting his research group at the National Taiwan University in 2008. His research interests include the design and synthesis of functional nanoporous materials for energy and biomedical applications. His research group also work on biomass valorization for fuel and chemicals production.

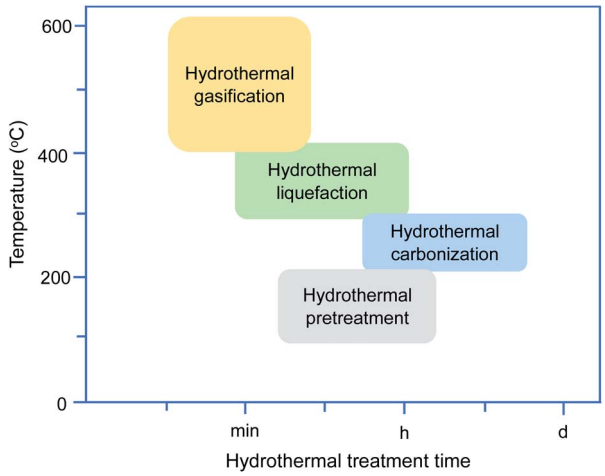

Fig. 1 Hydrothermal treatment under various temperatures and times. Reproduced with permission from ref. 42, copyright (2015) Elsevier.

carbon surface structure can be changed easily by introducing N, which provides more active sites for ion adsorption, increases bonding between sulfur and carbon, and improves the electrocatalytic activity.[20] Furthermore, it enhances the electron transfer ability of the carbon material and activity for oxidation reaction, for example, the oxidation of alcohols into aldehydes with very high selectivity over an NPC catalyst.[21] Additionally, the pore size and specific surface area of NPCs altered easily. The N content can be changed, suggesting that synthesis of NPCs is an important research topic because of their tunable properties and numerous applications. Consequently, N-doping is an excellent approach to improve the physicochemical properties and energy storage capabilities of porous carbons.

The N-doping in the carbon framework was performed easily because of the similarity of the covalent radius of carbon (0.77 Å) and nitrogen (0.74 Å) atoms.[22] However, N has higher electronegativity (3.04) than carbon (2.55), which consequently results in a change in the electronic structure of the carbon network. The N-doping offers additional electrons producing surface basicity, which improves catalytic performance in the oxidation reaction. The N is present in various forms, such as pyridinic (N-6), pyridine-N-oxide (N-*x*), pyrrolic (N-5), and quaternary N/graphitic N (N-Q). Among these N-types, the pyridinic N provides active sites for the oxygen reduction reaction (ORR).[23,24] Even metal-free NC catalysts are highly functional for the ORR, offering superior durability under acidic conditions. Moreover, NPCs are an excellent cost-effective alternative to expensive Pt/C catalysts. Consequently, for electrochemical energy storage applications, significant attention was provided for the synthesis of NCs with various N contents and types of N functionalities. NCs find applications as catalysts and supports for metal-supported catalysts, electrode materials for lithium-ion batteries and supercapacitors (SCs), and catalysts for the ORR and HER.[20,25]

The utilization of NPC has many advantages over porous carbon. For example, the incorporation of N increases wettability and hydrophilicity. Hence, many efficient methods have been investigated for the fabrication of NPCs.[3,16,20,26–28] Several NPC synthesis methods employed corrosive NH_3 as the N source with elevated temperature.[21] To overcome this issue, for the synthesis of NCs, sustainable and readily available renewable carbon and N precursors were utilized from biomass.[29] Although NCs are fabricated from inexpensive sources such as biomass, controlling their physicochemical properties (porous structure, N-type, and N-content) is difficult. Therefore, it is necessary to study the effect of various biomass sources on the synthesis of NCs and their properties. The synthesis of porous carbons from biomass has been described in detail elsewhere.[30,31]

To the best of our knowledge, no review articles have covered all aspects of biomass-derived NPCs and their applications in catalysis and energy storage. The present review aims to fill the gap in this active research field. In this review, we summarize various synthesis methods of biomass-derived NPCs. The applications of NPCs for catalysis and energy storage are also reviewed based on the physicochemical properties of NPCs and biomass sources.

2. Synthesis methods for NPCs

For the preparation of NCs, typically, two methods are employed. In the first method, the NC synthesis involves high temperature and N precursors, such as ammonia, urea, or amines, pyrrole, and acetonitrile.[32] In the second method, NCs are prepared using an *in situ* functionalization approach. In this method, carbohydrates containing nitrogen-functional groups, such as glucosamine or chitosan, are employed as carbon and N precursors.[28,33,34] Furthermore, N-containing molecules, such as amino acids or proteins, are also employed.[35] Although these N precursors have been used extensively for the synthesis of NCs, biomass as a N and a carbon precursor is preferred because biomass is not only an environmentally friendly renewable source but is also abundantly available.

In the present review, we mainly focus on the synthesis of NCs derived from biomass and their applications. Various synthesis methods for NCs are described in detail below.

2.1 Hydrothermal carbonization

Hydrothermal carbonization (HTC) is a conventional method used for the synthesis of carbonaceous materials. Friedrich Bergius discovered HTC in 1911. Initially, peat was used as a carbon source in HTC, resulting in the formation of a large quantity of CO.[36] The carbonaceous residue obtained in this process mimics coal formation. The HTC process was rediscovered at the beginning of the 21st century and employed for monosaccharides to obtain carbon microspheres.[37] The use of biomass as a carbon feedstock in water under mild temperature (180–250 °C) in a closed system results in the formation of a solid product instead of decomposition into gases.[38] Although HTC has been used extensively for the synthesis of NPCs, so far the chemistry of NPC production *via* the HTC process has not been well understood.[36] Consequently, to explore the real

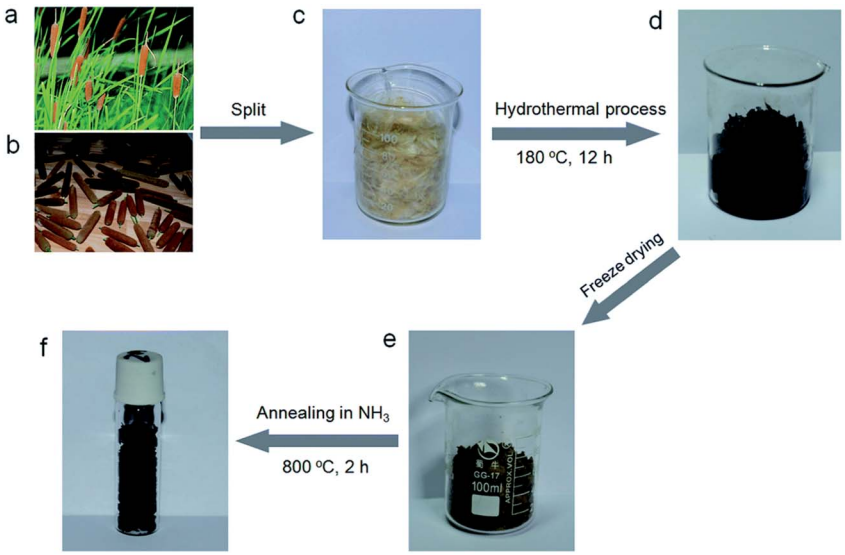

Fig. 2 Synthesis of the N-doped nanoporous carbon nanosheets. (a) Images of the Typha orientalis plant, (b) flower spikes, (c) raw material used for HTC, (d) carbonaceous hydrogel, (e) carbonaceous aerogel and (f) product NCS-800. Reproduced with permission from ref. 49, copyright (2014) RSC.

applicability of the HTC process on a large scale, additional research is required with various carbon sources (lignin, cellulose, glucose, and chitin). Comprehensive characterization is also necessary to address the fundamental chemistry behind this complex process.

The HTC method can be classified, depending on the temperature used in the process, as (1) high-temperature HTC and (2) low-temperature HTC. The low-temperature HTC process is often performed below 250 °C while the high-temperature HTC process is usually performed above 250 °C.[39] The high-temperature HTC method has been employed extensively in recent years to synthesize NC, N-doped graphene, and N-doped carbon nanotubes.[40] Hydrothermal gasification and hydrothermal liquefaction become competitive processes with an increase in HTC processing temperature, which results in a decrease in the formation of the desired products.[33,41] For the functionalization of carbon materials, the atom economy is higher in the case of low-temperature HTC.[28] As shown in Fig. 1, shorter HTC treatment time is required at higher temperatures due to higher reaction rates at a higher temperature.[42]

Typically, for the synthesis of NCs, N-containing biomass-derived chitosan and glucosamine were used.[43] Zhao *et al.* reported a green sustainable alternative method for the synthesis of NCs under mild reaction conditions.[28] In this method, hydrothermal treatment of biomass-derived chitosan and D(+)-glucosamine hydrochloride carbohydrates containing N and carbon was performed at 180 °C. These samples were calcined at 750 °C under a N_2 atmosphere to give N-containing carbon derived from chitosan and glucosamine. For comparison with carbons without N-doping, D(+)-glucose was used to synthesize carbon using a similar method. The elemental analysis result showed that NC derived from chitosan has 9.0 wt% N and 59 wt% carbon content, higher than that of pure chitosan (32.8 wt%), while NCs derived from glucosamine and glucose have *ca.* 65 wt% carbon and 6.8 wt% N, suggesting that during HTC, the carbon content increases due to the loss of hydrogen and oxygen in the dehydration process of carbohydrates, while the N concentration remains constant. In this method, neither metals nor surfactants were applied to catalyze the reaction. However, the N-containing carbon exhibited a very low BET specific surface area (10 $m^2\ g^{-1}$), and no porosity was detected.

For improving the HTC process, acidic conditions were employed, which helps hydrolysis of polysaccharides to sugar monomers and further dehydration of sugars into furans.[10,44,45] Moreover, during the HTC process, decomposition of sugars to furans (HMF and furfural) happens along with the formation of a small quantity of levulinic acid.[33] This organic acid further self-catalyzes the dehydration reaction of sugar monomers. Besides, using a desirable catalyst will promote the HTC process by decreasing the reaction time and temperature required for the HTC process.

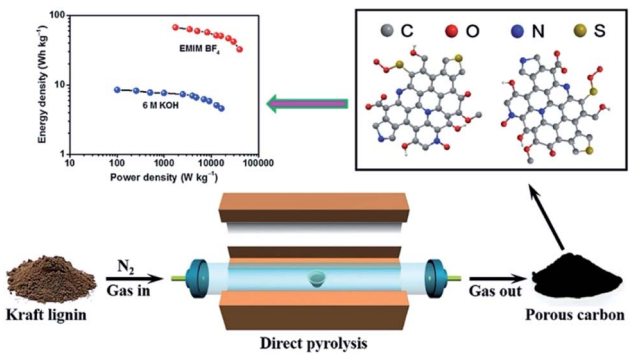

Fig. 3 Direct conversion of Kraft lignin to ONS-HPCs. Reproduced with permission from ref. 54, copyright (2019) Elsevier.

Table 1 Biomass-derived NCs prepared by pyrolysis and activation methods

Entry	Biomass	Pretreatment/ N-source	Carbonization/ activation conditions	Activation/ activating agent	Specific surface area ($m^2\ g^{-1}$)	Pore-volume ($cm^3\ g^{-1}$)	N-content (wt%)	Ref.
1	Kraft lignin	—	400 °C, 1 h 800 °C, 1 h, N_2	—	1307	0.66	1.35	54
2	Crushed wheat straw	$CaCl_2$, melamine & ethylene glycol, 2 h stirring, drying	800 °C, 2 h, N_2	—	892	0.65	5.63	55
3	Kraft lignin	H_2SO_4, 80 °C, 6 h	750 °C, 2 h, N_2	KOH	2762	1.32	1.06	78
4	Human hair	—	300 °C, 1.5 h, Ar	KOH, 800 °C pyrolyzed	1306	0.38	4.74	79
5	Wood waste	Urea	Ball milling 0.5 h, 800 °C, 1 h N_2	K_2CO_3	3000	2	4	80
6	Bagasse	Impregnated in water, 80 °C, 4 h. Urea	800 °C, 2 h, N_2	$CaCl_2$	805	0.68	8.9	81
7	Soybean residue + glucose	HTC, 200 °C, 15 h	800 °C, 1 h, N_2	KOH	2130	0.92	1.6	75
8	Soya chunks	300 °C, 3 h, Ar	1000 °C, 2 h, Ar	NaOH, 600 °C	1072	0.30	4.3	76
9	Potato waste	Melamine	700 °C, 2 h, N_2	$ZnCl_2$	1052	0.61	6.2	82
10	Chitosan + CH_3COOH	Urea	800 °C, 2 h, Ar	—	176	—	10.29 at%	83
11	Chitin/graphene oxide film	—	800 °C, 2 h, Ar	—	117	—	6 at%	84
12	Chitosan + $FeCl_3$	80 °C, 16 h, H_2O	800 °C, 2 h, Ar	—	543	—	3.15 at%	85
13	Glucose	Melamine	800 °C, 1 h, Ar	13.3 g $ZnCl_2$	1017	1.41	15.4	86
14	Glucose	200 °C, 8 h, H_2O, poly(ionic liquid)s with nitrile	550 °C, N_2	$Na_2B_4O_7$	424	0.89	5.3	87
15	Taro stem–NaOH mix (mass ratio = 1 : 4)	800 °C, 2 h, Ar, melamine	800 °C, 1 h, Ar	—	1012	0.53	4.8 at%	88

The HTC carried out with carbohydrates has three main stages: (1) dehydration of carbohydrates to furans, (2) polymerization of furans into polyfurans, and (3) further intermolecular dehydration.[46] The presence of metal helps to accelerate the HTC leading to a decrease in carbonization time. Iron oxide and iron are used for accelerating the HTC of starch.[47] The carbonization of glucose using iron nitrate was demonstrated by Guobin *et al.* for synthesizing carbonaceous spheres embedded with well-dispersed iron oxide nanoparticles under mild conditions.[48] The iron nitrate used in this process turns into the corresponding oxide during the HTC process. Iron oxide nanoparticles seldom aggregate compared to other metal nanoparticles because they exhibit covalent bonding instead of metallic bonding.

Chen *et al.* reported N-doped nanoporous carbon nanosheet synthesis using Typha orientalis (plant) for the oxygen reduction application.[49] The nanoporous carbon sheet has a high N content (9.1 wt%) and a large specific surface area (898 $m^2\ g^{-1}$). As shown in Fig. 2, for the synthesis of this NC nanosheet, hydrothermal treatment was performed first at 180 °C (12 h) for splits of the flowers of Typha orientalis to obtain a carbonaceous hydrogel. The obtained carbonaceous hydrogel was immersed several times in water to remove soluble impurities. The material was then freeze-dried for 24 h followed by annealing using NH_3 at 800 °C to 2 h with a heating and cooling rate of 5 °C min^{-1} resulting in the formation of the NC nanosheet. During the annealing process using NH_3, carbonization occurred. Subsequently, the NH_3 acts as a N source to form an N-doped nanoporous carbon nanosheet. The NH_3 also helps to etch the carbon, which results in the formation of nanopores. This material contains a higher content of pyrrolic and pyridinic N atoms. The increase in annealing temperature from 750 to 850 °C leads to an enhancement in BET specific surface area from 692 to 898 $m^2\ g^{-1}$. Besides, it increases the total pore volume from 0.36 to 0.52 $cm^3\ g^{-1}$ and decreases the micropore volume from 0.27 to 0.16 $cm^3\ g^{-1}$. This material provides an exceptionally high electrochemical activity for the ORR in acidic and alkaline solutions. The preparation of the N-doped nanoporous carbon was possible without using any templating or chemical and physical activation. The biomass-derived renewable carbons obtained *via* this method are ideal candidates for the synthesis of NC catalysts. The employment of a facile method for the synthesis of nanoporous carbons with higher N content and large specific surface area is crucial. Hence, more efforts are invested in the preparation of these types of material using biomass sources.

2.2 Pyrolysis

The pyrolysis method was used extensively for the synthesis of functional NPCs.[50–52] Yang and co-workers reported a simple way of synthesizing NC using sodium alginate and 1,6-hexanediamine.[53] In this method, initially, an aqueous solution

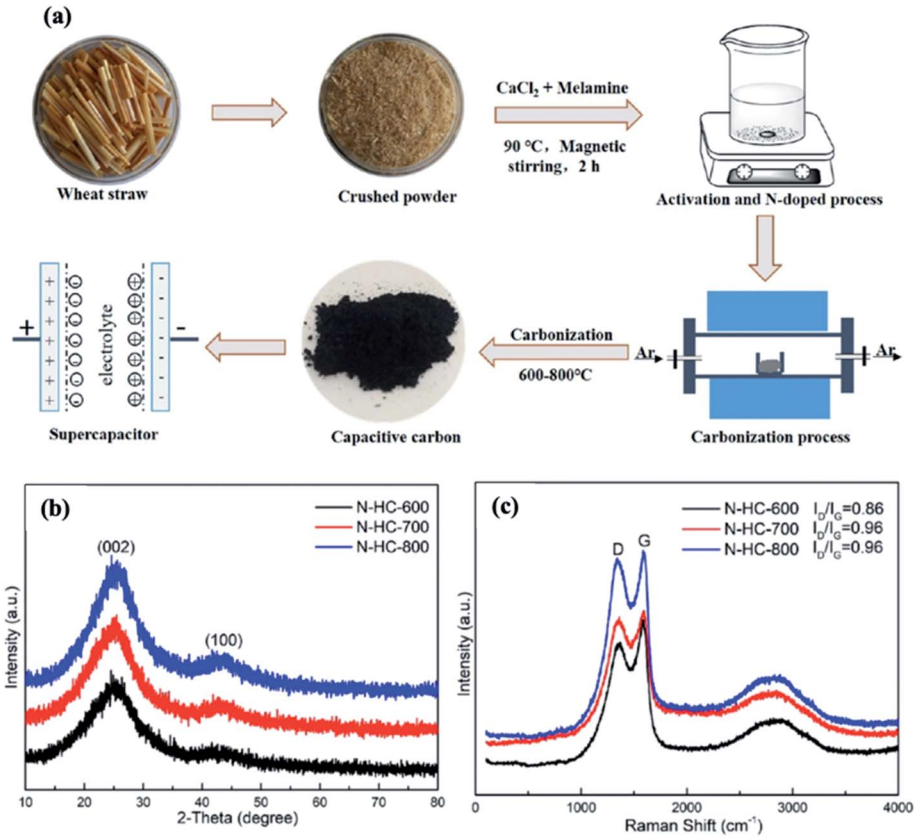

Fig. 4 (a) Synthesis of N-HPC using wheat straw. (b) XRD and (c) Raman spectra of N-HPC. Reproduced with permission from ref. 55, copyright (2018) ACS.

containing 1,6-hexanediamine, urea, and acetamide was added in the aqueous solution of sodium alginate followed by heating at 60 °C. After removing water, the mixture was pyrolyzed at 800 °C in the presence of N_2 to obtain NC. The prepared NC catalyst exhibited superior catalytic activity for the aerobic oxidation of amines to their corresponding imines.[53] The 1,6-hexanediamine during combustion produces toxic oxides of N, and it is also corrosive to tissue and metals, so it is necessary to utilize environmentally friendly precursors for the synthesis of NC. Lee *et al.* reported flexible synthetic strategies to obtain HPCs from bioethanol lignin and Kraft alkaline lignin.[50] In the case of bioethanol lignin, both KOH and NaOH were necessary to obtain the HPC. The addition of only KOH results in the formation of only micropore structures. This study showed that

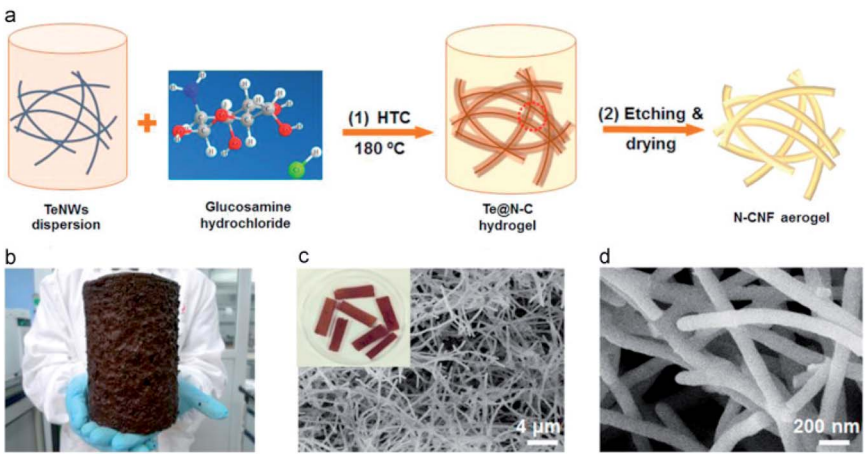

Fig. 5 (a) HTC synthesis of NC nanofiber aerogels using tellurium nanowires as a template, (b) large scale product quantity, and (c and d) SEM images at various magnifications. Reproduced with permission from ref. 58, copyright (2019) MDPI.

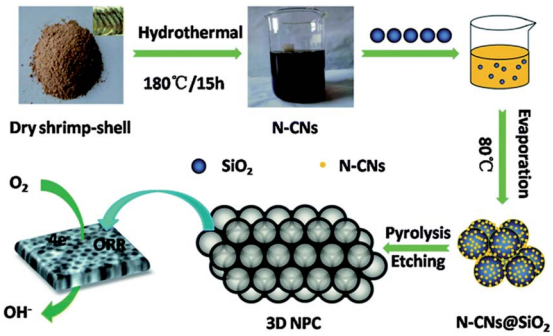

Fig. 6 Synthesis of shrimp-shell-derived N-doped carbon nanodots *via* a silica-assisted template process. Reproduced with permission from ref. 59, copyright (2016) RSC.

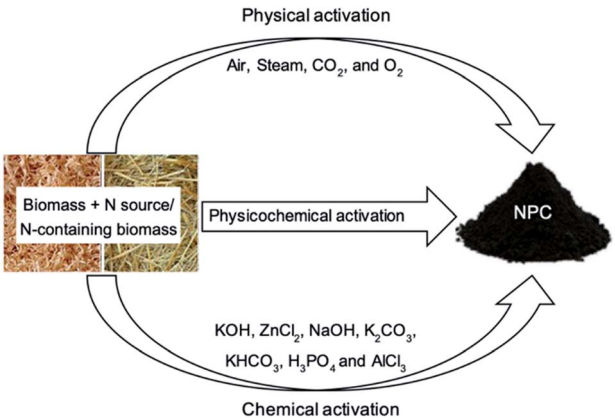

Fig. 7 Activation methods to produce NPCs.

using KOH as a pore-forming agent in the presence of NaOH results in the formation of a eutectic mixture of NaOH/KOH because of KOH and NaOH interactions, while in the case of Kraft alkaline lignin, addition of only KOH leads to the formation of HPC because of the presence of intrinsic NaOH in Kraft alkaline lignin. Consequently, for the synthesis of N-doped HPC, the addition of NaOH and KOH can be employed with N-containing biomass.

As shown in Fig. 3, Liu *et al.* demonstrated the synthesis of N, O, and S co-doped hierarchical porous carbon (ONS-HPC) using pyrolysis of Kraft lignin.[54] The Kraft lignin was directly pyrolyzed at 400 °C (1 h), and at a further increased temperature from 600 to 900 °C for 1 h under a N_2 atmosphere (Fig. 3 and Table 1, entry 1). After pyrolysis, the obtained black solid was washed with HCl solution to get rid of the inorganic impurity. Interestingly, the Kraft lignin impurities ($Na_2CO_3 \cdot Na_2SO_4$, NaCl, and KCl) play a crucial role in hierarchical carbon pore formation.[54] This study showed that the hierarchical pores are generated by the Na_2SO_4 that can react with the carbon during carbonization to form Na_2CO_3, which can act as an activating agent for hierarchical pores. The N_2-sorption analysis of ONS-HPCs indicated a type VI isotherm and the existence of micro-, meso- and macropores. The BET specific surface area was lower (338 $m^2\ g^{-1}$) for the sample pyrolyzed at 600 °C, while it was considerably increased to 1307 $m^2\ g^{-1}$ for the sample pyrolyzed at 800 °C. The ONS-HPC electrode exhibited high specific capacitance (244.5 F g^{-1}) when used for the SC application in 6 M KOH at 0.2 A g^{-1}. These results showed the effective utilization of lignin to synthesize heteroatom-doped HPCs with excellent properties, such as higher specific surface area, 3D framework, and doping of various heteroatoms. Although lignin is converted into a highly active electrode material using a simple method, further study is required to explore large-scale electrode production for energy storage devices and catalysis applications.

Wei *et al.* demonstrated N-doped hierarchical porous carbon (N-HPC) synthesis from wheat straw, as shown in Fig. 4.[55] For synthesizing N-HPC, oven-dried wheat straw (1.5 g), melamine (1.5 g), and $CaCl_2$ (1.5 g) were mixed in ethylene glycol (25 mL) and then the solution was stirred at 90 °C (2 h). The solution was heated in a vacuum oven at 110 °C to obtain a solid mixture. Finally, as shown in Fig. 4, the obtained solid was calcined at 600 to 800 °C under a N_2 atmosphere for 2 h. An acidic solution (1.5 M HCl) and Millipore water were used to wash the prepared material; then it was dried at 70 °C in a vacuum oven for 24 h to obtain N-HPC.

The N-HPC sample produced at 800 °C offers a high BET specific surface area (892 $m^2\ g^{-1}$), more micropores, and 5.63 wt% N content (Table 1, entry 2). The XRD characterization showed two diffraction peaks for 001 and 002 planes, which indicate graphitic carbon.[55,56] As presented in Fig. 4(b), the N-HPC showed a slight graphitic nature because of the low intensity of the diffraction peak at 43°. The first broad peak ($2\theta = 25°$) indicated an amorphous structure. The Raman spectra exhibited the presence of a G-band, which corresponds to the graphitic structure due to stretching vibrations of the C–C bond in sp^2 hybridization with E_{2g}.[57] The Raman spectra (Fig. 4(c)) showed an increase in the I_D/I_G values from 0.86 to 0.96, with an increase in pyrolysis temperature from 600 to 800 °C, suggesting an increase in defects and edges in the material. The scanning electron micrograph (SEM) implied that N-HPC-600 has few noticeable pores while N-HPC-700 and N-HC-800 exhibited a 3-D honeycomb porous structure.[55] The interconnected pores have thin walls, which can accelerate the electrolyte transmission upon using electrode materials. All these carbon materials produced using the pyrolysis method have a hierarchical pore structure, and their BET specific surface area increases from 552 (600 °C) to 657 (700 °C) and 892 $m^2\ g^{-1}$ (800 °C) with increasing pyrolysis temperature. Consequently, the N content decreases with increasing pyrolysis temperature.

In the electrochemical measurement study, N-HPC-800 showed a superior current response when used as an electrode material in 6 M KOH solution (three-electrode system, scan rate 30 mV s^{-1}), suggesting that N-HPC-800 has improved charge storage ability compared to other samples because of its higher specific surface area. The higher surface area and N doping played a vital role in improving electrochemical performance. Hence, the synthesis of NC materials has a significant importance.

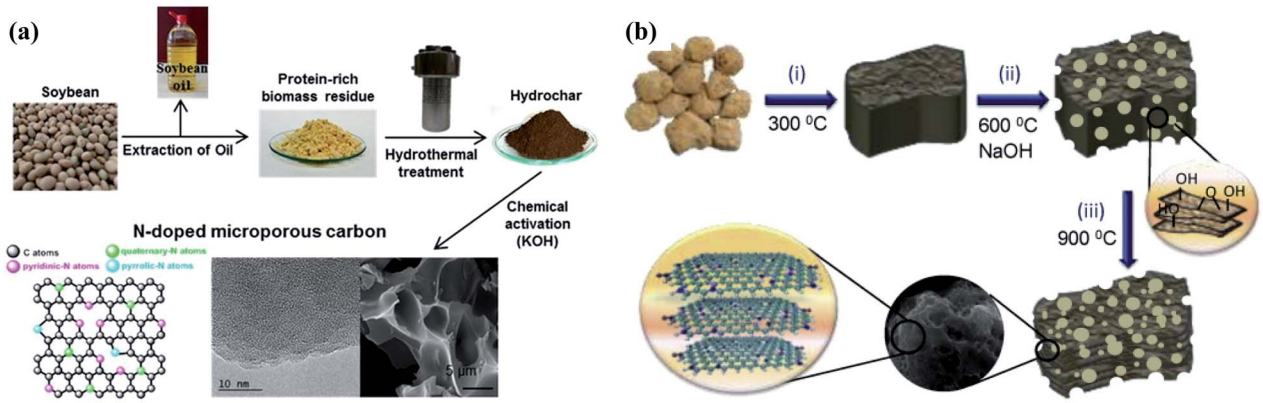

Fig. 8 (a) Synthesis of N-doped microporous carbon using a protein-rich biomass residue derived from soybean. Reproduced from ref. 75, copyright (2015) Sci. Rep. (b) Schematic of the synthesis method for soy-derived NC using NaOH as an activating agent. Reproduced with permission from ref. 76, copyright (2017) Elsevier.

2.3 Template directed synthesis

To overcome the drawbacks of lower porosity and a decrease in N content during the pyrolysis process, other methods such as templating, chemical/physical activation, and sol–gel methods were employed to synthesize NCs. The template directed synthesis process for NPCs was extensively implemented using biomass because of its ability to prepare ordered porous NCs. NCs with well-ordered pores and desirable physicochemical properties were synthesized using template-directed synthesis. In this method, the template helps to form pores and promotes structural ordering during the carbonization process.

Recently, for the synthesis of NC nanofiber aerogels, a template-directed HTC process was used.[58] In this case, tellurium nanowires serving as a template and a N-containing carbohydrate, *i.e.* glucosamine, serving as a N source were utilized to synthesize NC aerogel with improved electrical conductivity. The synthesis method is illustrated in Fig. 5, and the advantage of this method over electrospinning is the ability to control the fiber diameters. However, the downside of this method is the higher cost of tellurium nanofibers used to direct the growth of the carbon nanofibers. To overcome this issue, alternative low-cost cellulose nanofibers and inorganic nanowires may be the right choice for the template as an economically feasible option. The CO_2 activation and higher temperature provide high porosity and conductivity. These NC nanofibers show excellent activity as electrodes for SCs and other electrocatalytic applications.

Liu *et al.* reported the synthesis of 3D-NPC using shrimp-shell-derived carbon nanodots for the ORR. The 3D-NPC was prepared using HTC with template-assisted pyrolysis, as shown in Fig. 6.[59] The N-doped nanodots derived from shrimp shells contain N and O-rich functional groups and smaller nanodot sizes in the range of 1.5–5 nm used as the N and O source. In this method, silica spheres (~200 nm) prepared by a Stöber method were used as a template. The N-CNs@SiO_2 composite was formed by mixing N-CNs and silica spheres followed by evaporation. Furthermore, the obtained N-CNs@SiO_2 was pyrolyzed followed by acid etching, resulting in the formation of 3D-NPC. The 3D-NPC obtained by pyrolysis treatment at 800 °C exhibited superior catalytic activity and high durability for the ORR, comparable to those of the Pt/C catalyst. The 3D-NPC electrocatalyst showed high methanol tolerance in alkaline media compared to a commercial Pt/C electrocatalyst.

2.4 Activation

Biomass-derived NCs were also obtained using chemical and physical activation methods or a combination of both. Physical activation requires air, CO_2, or steam as an activating agent. In chemical activation, various chemical activation agents are utilized, such as KOH, NaOH, $ZnCl_2$, K_2CO_3, $KHCO_3$, H_3PO_4, and $AlCl_3$ (Fig. 7).[14,50,60–62] The use of air in physical activation suffers from the exothermic reaction of carbon with the oxygen present in air, which makes it difficult to control the reaction, leading to burning and a decrease in the carbon yield. Nevertheless, the use of air makes the process economically viable because the higher activity of oxygen results in lower activation energy than when CO_2 and steam are used as activating agents. For example, the gasification of pyrolyzed coals in air and CO_2 was performed at 380 and 800 °C, respectively.[52] In the case of air gasification, initially, the pore volume and specific surface area increased rapidly. After reaching a certain level, the surface area and micropore volume did not change noticeably with the carbon conversion. However, in the case of CO_2 activation, with the progress of gasification, the volume of micropores and specific surface area increased noticeably. The air activation provides a wide pore size distribution compared to the CO_2 activation.[52] In practice, mostly CO_2 and steam activating agents are selected instead of air. The steam requires lower operation temperature compared to CO_2 because of its higher reactivity.

In chemical activation, various chemical agents are commonly used, such as KOH, H_3PO_4, and $ZnCl_2$. The KOH acts as an oxidizing agent while H_3PO_4 and $ZnCl_2$ perform the dehydration reaction.[52] In the chemical activation process, typically, the carbon precursors were heated with activating agents under temperature in the range of 400 to 900 °C. The

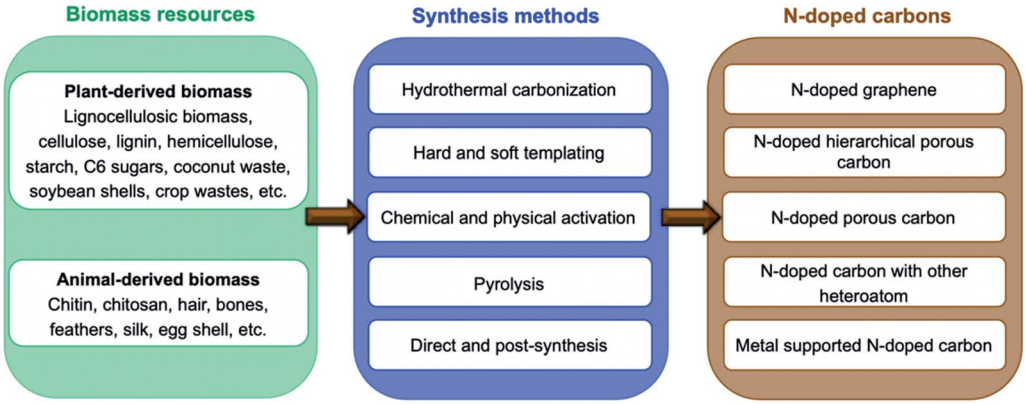

Fig. 9 Biomass resources, synthesis methods, and various N-doped carbons prepared from biomass.

activation agent improves the specific surface area and porosity by comprehensive action and synergistic effects, including carbon lattice expansion and chemical activation due to metallic intercalation.[63] The use of the H_3PO_4 activation agent generates heterogeneity in the micro-porosity, while the use of $ZnCl_2$ yields micropores with uniform size because of its hydrates or smaller size.[64] KOH acts as an oxidizing agent, and it helps to oxidize the carbon into carbonate ($6KOH + 2C \leftrightarrow 2K + 3H_2 + 2K_2CO_3$), leading to pore formation in the carbon framework due to etching. Furthermore, porosity can be achieved by decomposition of K_2CO_3 into CO_2 *via* gasification above 700 °C. Moreover, higher reactivity leads to lower gasification temperatures for porosity development.[52,65,66] The optimal temperature for porosity depends on the carbon precursor and type of activating agent. An increase in temperature above the optimal limit leads to a decrease in porosity due to collapsing of the structure or shrinkage issues.[52,67–69] The KOH activation offers higher pore-volume and high surface area compared to activation with other activating agents.[70–72] Furthermore, the KOH activating agent also provides a narrow pore size distribution, which can be tuned by controlling the activation parameters (temperature, time, and amount of KOH). The H_3PO_4 and $ZnCl_2$ chemical agents provide a broad pore size distribution.[52,72–74] In Table 1, various examples of biomass-derived NCs prepared by pyrolysis and activation methods are presented.

Ferrero *et al.* reported soybean residue for the synthesis of NC using HTC and the KOH activation method, as shown in Fig. 8(a).[75] The defatted soybean, a protein reach biomass, was used for the HTC treatment followed by KOH activation. The obtained NC had a large BET specific surface area ($S_{BET} = 2130$ m^2 g^{-1} for 800 °C activation temperature) and exhibited high capacitive performance in an aqueous electrolyte with superior specific capacitance (Table 1, entry 7). Rana *et al.* demonstrated the synthesis of soya derived NCs using NaOH activation followed by pyrolysis for SC, ORR, and CO_2 capture applications. This soya derived N-doped catalyst exhibited a 1072 m^2 g^{-1} BET specific surface area and showed excellent performance for the SC application (Table 1, entry 8). As illustrated in Fig. 8(b), the synthesis of soya derived NC has three steps: (i) pre-carbonization, (ii) activation, and (iii) pyrolysis. The pre-carbonization of soya chunks at 300 °C results in the evaporation of fatty acid and water. The activation using NaOH at 600 °C under an inert atmosphere provides oxygenated functional groups and disrupts the lamellar-like features, which result in the formation of a porous material with an increase in BET surface area. Furthermore, this obtained material is pyrolyzed at various temperatures (800–1000 °C) to achieve NC.

Chemical activation has various advantages over physical activation such as (1) use of lower pyrolysis temperature, (2) high carbon yield and surface area, and (3) easy tuning of microporosity. Hence, chemical activation methods are studied extensively for the synthesis of NPCs. Some reports showed physicochemical and microwave-induced activation,[77] but physical activation methods with biomass are comparatively insufficient.

KOH has been used extensively as an activation agent for biomass-derived NC and porous carbons. Fan *et al.* reported the fabrication of NC by a chemical activation approach in which K_2CO_3 and chitosan were used as the activation agent and precursor, respectively.[62] The physicochemical properties of NC were tuned by altering the K_2CO_3/chitosan ratio and activation temperature. A sample prepared with K_2CO_3/chitosan = 2 at 635 °C calcination temperature under ambient conditions showed high CO_2 uptake. This material showed a large BET specific surface area of 1673 m^2 g^{-1}, and an increase in calcination temperature from 600 to 800 °C resulted in an increase in surface area from 1180 to 2567 m^2 g^{-1}. In contrast, an increase in calcination temperature showed decreased N content for the samples prepared with K_2CO_3/chitosan ratios of 1 and 2.[62]

2.5 Direct and post synthesis

In this section, the synthesis of NCs using additional methods is discussed, including chemical vapor deposition (CVD), layer separation growth, and arch discharge. These methods are called direct synthesis methods.[89,90] On the other hand, post-synthesis methods include thermal annealing, bombardment, or solution treatment.[91] Recently, NPC functionalization has been extensively studied to improve the properties of these

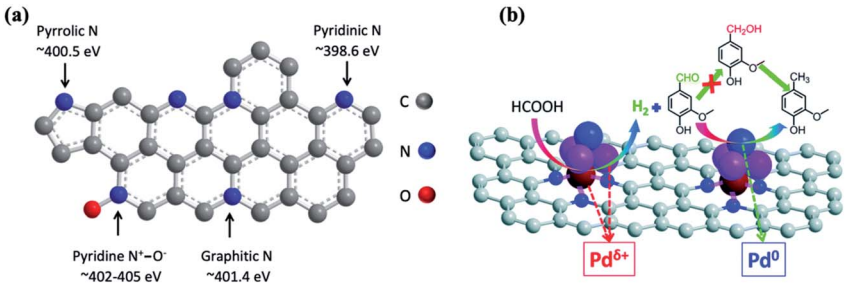

Fig. 10 (a) The commonly doped N species in graphitic carbons with the corresponding reported X-ray photoelectron spectroscopy (XPS) binding energies.[103] (b) Possible reaction mechanism of transfer HDO of vanillin over Pd@MNC. Reproduced with permission from ref. 86, copyright (2017) RSC.

materials for practical applications. Giuliano and coworkers reported NC nanotube functionalization using chemical functionalization and CVD to reveal the electrochemical role of specific N-functionalities in the ORR.[92] Although the synthesis of N-doped graphitic carbons using the CVD method has been widely reported, this method is not affordable and is difficult to use on a large scale. The N content reported for CVD is lower, which precludes its commercialization. However, the solvothermal method is relatively affordable, and the preparation of NCs is carried out under mild conditions on a large scale. Furthermore, higher N-doping (4–17%) is also possible using this method.[93] In CVD, a metal catalyst is used for the synthesis of N-doped graphene under high temperature from carbon (*e.g.*, ethylene, methane) and N sources (ammonia) or a liquid precursor containing carbon and N such as acrylonitrile or pyridine. These N and carbon precursors dissociate under high temperatures and recombine to form N-doped graphene or N-doped graphite on the surface of the catalyst. Besides, for the synthesis of P-doped graphite and B-doped carbons, the CVD method was reported.[94]

The other approach used for the synthesis of N-doped graphene and NC nanotubes is an arc discharge method.[95] In this method, graphite is typically vaporized along with a N precursor (pyridine or NH_3) to obtain N-doped graphene. In the bombardment method, such as plasma treatment, the N-doping was controlled by varying the exposure time and plasma strength. However, in this method, oxygen functionalization happens to a greater extent.[96] ILs are sometimes used in combination with a hard template to prepare controlled porous materials. ILs have beneficial properties such as non-flammability, low vapor pressure, and excellent electrical conductivity; the low vapor pressure of ILs enables carbonization without evaporation.[97] Several studies also reported the possibility of using ILs in the absence of a template. However, in this method, the materials are obtained with a lower specific surface area.[93,98] The biomass resources and methods used for the synthesis of NCs are summarized in Fig. 9. The ash content of biomass can affect the thermochemical processes; for example, Si is relatively inert under pyrolysis. Inorganics, including K, Na, Ca, and Mg, catalyze the thermal degradation of biomass to light gases.[99] The presence of higher ash content in biomass adversely affects the pyrolysis process. Consequently, ash removal from biomass is sometimes necessary. For ash removal from biomass, anatomical fractionation, size fractionation, and air classification strategies have been employed.[99] The air classification strategy is the most effective for removing ash from biomass.

3 Applications of nitrogen-doped carbons

3.1 Catalysis

Homogeneous transition metal complex catalysts offer significant advantages in catalysis because of their tunable properties at the molecular level for specific applications; moreover, the synthesis of these catalysts was reproducible. Although the properties of metal complexes are easily modified, they suffer from drawbacks, such as low stability and difficulty in recycling from the reaction mixture because of their homogeneous nature. On the other hand, heterogeneous catalysts are readily separated from the reaction mixture and can be employed efficiently for continuous flow processes. Hence, to overcome these issues of homogeneous transition metal complexes, homogeneous catalysts are anchored on a heterogeneous support to make them heterogeneous catalysts. Besides, the activity of anchored metal complexes can be improved compared to that of homogeneous catalysts. The porous carbon and NPCs often act as supports for anchoring various metal complexes and catalyst precursors by covalent bonds than just physical adsorption, which precludes leaching of the metal in the reaction medium. Besides, the carbon material offers the possibility of tuning the surface structures readily by N introduction or by thermal and chemical post-treatment methods followed by functionalization.[100] The modification of the NC support is beneficial for introducing various functional groups (–COOH, –OH, and $–NH_2$) for creating anchoring sites for metal complexes. In the case of a supported metal catalyst, the activity mainly depends on the metal distribution and metal loading on the NC support. The carbon surface functional groups offer anchoring sites to the metal precursors. They also hinder metal agglomeration by reducing the migration of metal crystallites. That leads to a decrease in metal sintering issues. Hence, control of the surface chemistry of the NCs is crucial for the

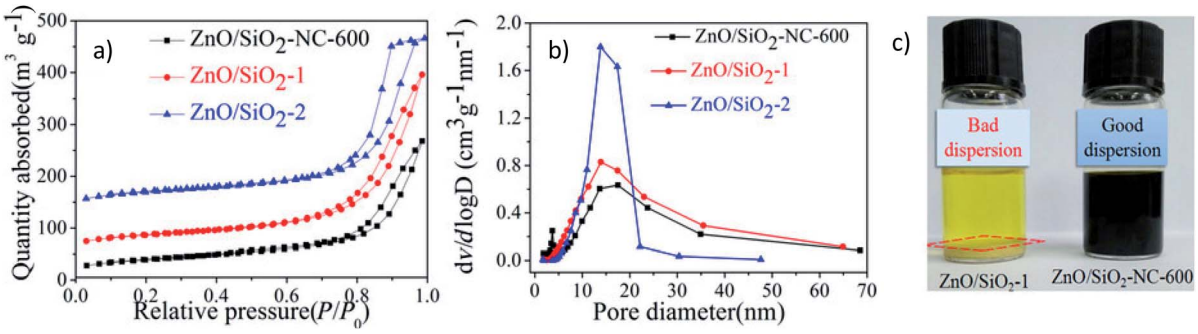

Fig. 11 (a) N_2 adsorption/desorption isotherms and (b) the pore-size distributions of the hybrids ZnO/SiO_2-NC-600, ZnO/SiO_2-1, and ZnO/SiO_2-2, and (c) dispersion of the catalyst in methanol at RT. Reproduced with permission from ref. 105, copyright (2017) Wiley.

synthesis of highly active and well-dispersed metal-supported catalysts.

Recently, NPCs were employed as supports for the synthesis of many metal-supported catalysts. They provide a higher surface area, and the porosity can be tuned to impart high stability and electrical conductivity. Metal-supported NPC catalysts were reported for various reactions, including Fischer–Tropsch synthesis (FTS), H_2 generation, oxidation, and reduction reactions. Significant progress has been made in metal nanoparticle catalysts modified using NC as the support. As shown in Fig. 10(a), the N-doping in the carbon matrix provides various types of bonding of the N dopant, including pyrrolic, pyridinic, graphitic, and pyridine N-oxide. The N-doping may result in defects in the graphitic lattice or generation of vacancies. The pyridinic N atoms are present in the vacancies in the graphitic carbon. In the carbon plane, by replacing the carbon atoms, the graphitic N atoms are located. Due to the diverse N bonding, N-doping enhances the physicochemical properties of metal-supported NC catalysts for various catalytic applications. The presence of interstitial N and C–N defect sites can improve the growth and nucleation of metal nanoparticles.[101]

For the transfer hydrogenation of vanillin, an acid-resistant Pd catalyst supported on biomass-derived N-doped mesoporous carbon (NMC) showed high activity (Fig. 10(b)).[86] The NMC support was prepared using glucose and melamine precursors and $ZnCl_2$ as a pore-forming agent. The Pd/NMC was prepared by dispersing $PdCl_2$ and NMC in water and stirring it for 30 min. Next, the solution was heated in a closed system at 40 °C for 8 h under H_2 (2 MPa), and the final catalyst was recovered *via* filtration. The Pd/NMC catalyst showed three times higher activity than the Pd/MC catalyst without N-doping for vanillin hydrogenation. The reactions were carried out in water using formic acid as the hydrogen donor. The result showed an exceptionally high activity. The vanillin completely converted into 2-methoxy-4-methylphenol at 150 °C (3 h). The NMC catalyst is stable in formic acid; the electron-deficient Pd concentration is affected by N-doping due to strong interaction between Pd and N, which results in the co-existence of metallic Pd and electron-deficient Pd. In this work, the NC acts as a support and also contributes to the increase in the catalyst activity. The surface-N can act as defect sites. It enhances the hydrophilicity and wettability of the catalyst. Higher the catalyst hydrophilicity, the more active it is for the HDO of vanillin in a polar protic solvent such as water. For vanillin hydrogenation, Yang *et al.* demonstrated a Co embedded biomass-derived mesoporous NC catalyst.[102] The Co@NC-700 catalyst exhibited >95% vanillin conversion with 99% 2-methoxy-4-methyphenol selectivity at 180 °C (4 h). Interestingly the Co@NC-700 catalyst showed 15.4 times higher activity compared to Co/AC.

Generally, for the synthesis of metal-supported NC catalysts, two methods were reported. The first one is the loading of metal on pre-synthesized NC using a deposition precipitation and impregnation method. The second method is the introduction of N and metal species simultaneously on the carbon. We have previously reported the synthesis of gold-nanoparticle embedded N-doped nanoporous carbon using the *de novo* approach. In this method, initially, the gold precursor was encapsulated in ZIF-8, and then it was reduced to gold nanoparticles.[104] A mesoporous Co encapsulated NC catalyst (Co@NC) was prepared by the one-pot carbonization of glucose, $CoCl_2$, and melamine.[102] The unique structure of Co@NC plays multiple roles in the catalytic transfer hydrogenation of biomass with formic acid (FA). The Co@NC exhibited excellent chemoselectivity and high yield for HDO of vanillin to 2-methoxy-4-methylphenol using FA as a reductant.

For the green synthesis of benzimidazoles, ZnO nanoparticles supported on silica and NC were explored by Chen *et al.* using silica gel and chitosan precursors.[105] The ZnO supported on SiO_2 and SiO_2-NC samples showed type-II isotherms and the presence of macropores and mesopores with low BET surface areas (Fig. 11(a)). The ZnO nanoparticles were well-distributed in the SiO_2-NC-600 and SiO_2-1 supports due to the presence of chitosan during the catalyst synthesis. On the other hand, ZnO/SiO_2-2 showed ZnO nanoparticle aggregation due to a narrow range of pore diameters (Fig. 11(b)). The ZnO anchored on a silica support and NC was well dispersed in MeOH compared to ZnO/SiO_2-1, as shown in Fig. 11(c). The NC in ZnO/SiO_2-NC-600 assisted the uniform dispersion of the catalyst in MeOH, resulting in enhanced contact between the nanoparticles and substrate that helps to improve the catalytic performance. The interaction between the NC support and ZnO might increase the acidic sites of the catalyst, resulting in enhanced catalytic performance. The amino and hydroxyl

groups of chitosan used as a precursor for catalyst synthesis assist the complexation of Zn salt that increases Zn ion dispersion. The SiO_2 support improves the surface area of the catalyst and stabilizes the formation of NC. The N atoms restrict the size of ZnO nanoparticles to the sub-nanometer level and increase the dispersibility. The ZnO/SiO_2-NC-600 catalyst showed high activity for the synthesis of 2-arylbenzimidazoles using diamines and aromatic aldehydes in MeOH under mild conditions.

3.1.1 Oxidation reactions. A metal-free NPC was used directly as a catalyst for many oxidation reactions.[106–111] Recently, our research group reported N-doped nanoporous carbon as a catalyst for the oxidation of HMF and furfural into FDCA and maleic acid, respectively.[106,112] The increase in graphitic-N (N-Q) species in an N-doped nanoporous carbon caused an improvement in the FDCA yield in the aerobic oxidation of HMF (11% FDAC yield, 600 °C (4% N-Q); 80% FDCA yield, 900 °C (24% N-Q)). Similarly, higher activity is observed for the oxidation of furfural into maleic acid with NC catalysts with a high content of N-Q species. In this study, the NC derived from biomass showed inferior activity due to the lower content of N-Q species. Hence, the synthesis of biomass-derived NC with higher content of N-Q species is necessary for the selective oxidation of biomass-derived HMF and furfural.

Zhang *et al.* demonstrated the aerobic oxidation of alcohols and hydrocarbons over a Pd@N-doped carbon catalyst without using a solvent.[87] In this method, the NC was first prepared from glucose by the HTC method, followed by carbonization at 550 °C. The catalyst contains 35.3, 39.6, and 25.1% pyrrolic, pyridinic, and quaternary type N, respectively. XRD analysis revealed the presence of broad and weak diffraction peaks at $2\theta = 25^\circ$ and 44°, attributed to the (002) and (100) planes of the graphite type lattice. The Raman spectra of NC exhibited a D band at 1355 cm^{-1} and a strong G band at 1586 cm^{-1}. The D and G band intensity ratio for N-doped C-Glu_A-550 (the subscript denotes the additive) is higher ($I_D/I_G = 0.78$) compared to that of C-Glu-550 ($I_D/I_G = 0.63$), indicating the presence of structural defects on the NC. Besides, NC exhibited a hierarchical porous structure and was selected as a support for the Pd embedded catalyst synthesis. The prepared Pd embedded catalyst showed 6 nm mean particle size of Pd nanoparticles; furthermore, the well-defined lattice fringes confirmed the (111) crystal plane of Pd. XPS analysis showed that the two asymmetric peaks correspond to Pd $3d_{5/2}$ and Pd $3d_{3/2}$. The dispersion of Pd calculated using CO adsorption is 33.5%. The Pd embedded catalyst (4%Pd@C-Glu_A-550) can only show a 5.7% indane conversion at 80 °C. However, an increase in reaction temperature to 120 °C showed an improvement in the indane conversion from 5.7 to 31%. Similarly, in the case of benzyl alcohol oxidation catalyzed by the Pd catalyst (0.5% Pd@C-Glu_A-550), 49% conversion was observed at 120 °C in the presence of air.

Recently, the oxidation reactions of biomass-derived furans were studied extensively using NC catalysts. For the selective oxidation of HMF to DFF, a chitosan derived NC catalyst was reported by Ren *et al.*, where the NC was obtained *via* a pyrolysis method from chitosan and urea served as the N precursor.[113] The oxidation of HMF into DFF over NC was carried out at 100 °C under 1 MPa O_2 pressure, and a catalytic amount of HNO_3 exhibited a high DFF yield (95%).[29] In this reaction, the catalytic activity depends on the type of N atom and the specific surface area of the catalyst. Besides, the catalytic activity increased with increasing pyrolysis temperature from 650 to 950 °C. Lin *et al.* described a chitosan-derived Co@NPC catalyst for the oxidative esterification of HMF to 2,5-furandicarboxylic acid dimethyl ester.[114] The catalyst performance was improved by the dual role of Zn, *i.e.*, self-sacrificial template and acid–base site regulator. The optimization of acidic and basic sites and enhanced specific surface area due to partial evaporation of Zn during the synthesis process from the catalyst resulted in the higher activity.

3.1.2 Hydrogenation reactions. A molybdenum oxide@N-doped carbon (MoO_x@NC) catalyst was demonstrated recently for the selective vapor-phase hydrodeoxygenation (HDO) of lignin-derived phenolic compounds.[115] MoO_x@NC was produced by *in situ* pyrolysis of preloaded cellulose and a molybdenum precursor ($(NH_4)_6Mo_7O_{24}\cdot 4H_2O$) under an NH_3 flow. The vapor phase HDO of guaiacol using the C-600 catalyst showed 35.6% guaiacol conversion with 10% aromatic hydrocarbons and a 19% yield of phenols. In contrast, the use of the NC-600 catalyst exhibited 54% guaiacol conversion with 16.7% aromatic hydrocarbons and 26.3% yield of phenols, suggesting an improvement in the catalyst performance due to N doping. Besides, the use of molybdenum oxide supported on NC catalysts for HDO of guaiacol resulted in complete conversion of guaiacol with 68.8% aromatic hydrocarbons and 6.7% phenols, indicating that the N-doping and presence of molybdenum oxide enhance the HDO of guaiacol and produce more aromatic hydrocarbons.

The incorporation of N into carbon can improve the stability and catalytic activity of the supported metal nanoparticles. The NC nanotube supported Pd catalyst showed high activity for the hydrogenation of nitrobenzene.[116] This study demonstrated, using XPS analysis and DFT calculations, how the metal-support-interaction influences the catalyst activity. The adsorbed Pd on N@CNTs donates electrons to pyridinic N, and this metal-support-interaction leads to electron deficiency in Pd. Hydrogenation of nitrobenzene indicated that the metal-support interaction can help in tuning the catalyst activity. The N-doping of carbon nanospheres on the nickel catalyst has a strong impact on reactant adsorption and metal sintering.[117] N-doping in the carbon nanospheres decreases the graphitic character of the catalyst, and the quaternary N provides an electron-rich carbon surface, which improves the mobility of the metal and consequent sintering.[118] The large particle size offers a higher reaction rate for butyronitrile hydrogenation by decreasing the nitrile group adsorption strength, which increases the activity for hydrogenation.

Recently, a Pd/NC catalyst was reported for the hydrogenation of benzoic acid to cyclohexane carboxylic acid.[119] The NC catalyst was prepared by HTC using glucosamine hydrochloride as a carbon and nitrogen precursor. For the chemoselective hydrogenation of benzoic acid, the Pd@NC catalyst showed 9 times higher activity than Pd@AC. Besides, the Pd@NC catalyst

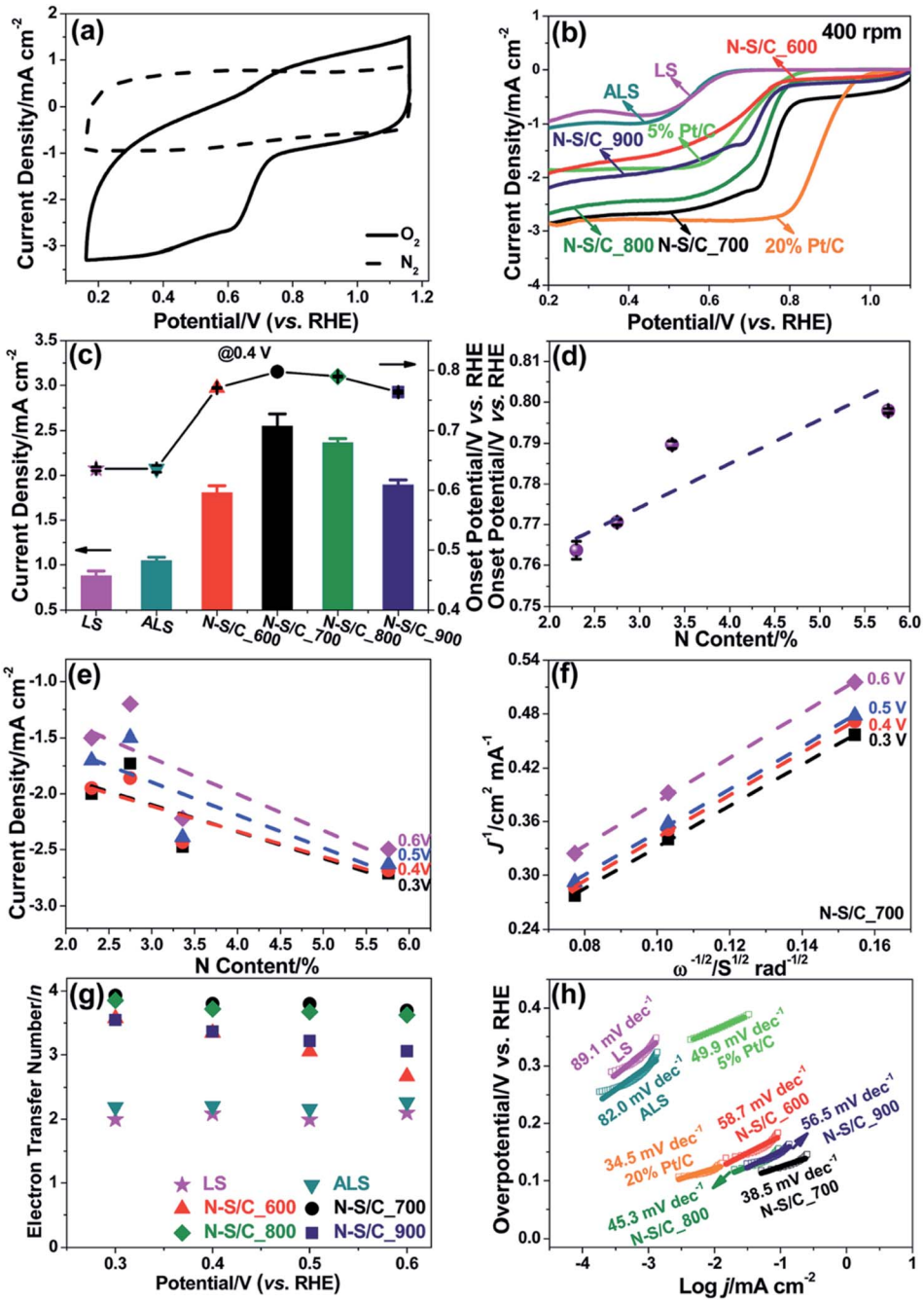

Fig. 12 (a) CVs of N-S/C_700 in N_2- (dashed line) and O_2-saturated (solid line) aqueous 0.1 M KOH at a scan rate of 100 mV s^{-1}. (b) LSVs of various catalysts obtained at 400 rpm and 5 mV s^{-1} in oxygen-saturated 0.1 M KOH. (c) Comparison of onset potential and current density at 0.4 V (*vs.* RHE) for catalysts. Correlation of (d) onset potential and (e) current densities at 0.6, 0.5, 0.4, and 0.3 V (*vs.* RHE) with N contents. (f) K–L plot derived from voltammograms at different rotation speeds. (g) Number of electrons transferred in the ORR. (h) Tafel plots, with the respective slopes indicated, for various catalysts extracted from the LSV results. Reproduced with permission from ref. 135, copyright (2018) RSC.

exhibited high activity towards hydrogenation of phenylacetic acid and benzoic acid derivatives, such as ethyl benzoate and benzamide.

As demonstrated in the above examples, the use of NCs alone as a catalyst resulted in enhanced activity and stability. Besides, the supported metals and metal oxides on NC help to improve the catalyst performance. The utilization of biomass as a carbon and nitrogen precursor for the synthesis of NPCs and its use for biomass conversion and other chemical transformations as a catalyst can offer high economic viability for large scale applications.

3.2 Energy storage

3.2.1 Fuel cell. Development in fuel cell research and various fuel cell technology applications helps to circumvent

the dependency on fossil fuels. Hence, fuel cell research has become an essential topic in academics and industry. The fuel cell directly transforms chemical energy into electricity with high efficiency of energy conversion without combustion processes. Additionally, it generates electricity in silent operation at a fixed position without forming harmful waste products. In a fuel cell, two half-reactions happen, one at the cathode and another at the anode. The electrodes are produced from porous carbon coated with a catalyst like Pt or Ni; alternatively, they can be polymer-electrolyte membranes (PEMs) made from composite membranes. The electrodes are separated by electrolytes such as aqueous KOH, and the fuel cells are classified based on the fuel and the type of electrolyte used. The hydrogen and the methanol fuel cells are the most widely studied fuel cells, and in both the fuel cells, the ORR is commonly the rate-determining step.[120] However, the ORR suffers from drawbacks such as requiring an overpotential. Usually, electrocatalysts are not stable under these conditions, creating a barrier to large scale fuel cell applications.

High electrocatalytic activity is reported for the Pt/C electrocatalyst. However, it is expensive and shows sluggish electron-transfer kinetics and inferior durability, making it unsuitable for commercial applications of fuel cells.[121] Hence, more attention has been focused on developing porous materials with supported non-precious metals or without metals as catalysts to enhance the electrocatalytic activity and stability. Recent studies on the electrochemical ORR using heteroatom (N, P, B, S, and Se)-doped metal-free porous carbons as electrocatalysts showed high activity and stability.[120,122–124] Consequently, these heteroatom-doped porous carbons can be a potential candidate to replace the expensive Pt-based catalysts.[125–127] The NCs have high thermal and electronic conductivity due to π-delocalization. Because of these properties, NCs have been employed extensively for the ORR. Furthermore, NCs showed high stability, superior ORR activity, and high methanol and CO poisoning resistance compared to Pt/C.[120,128]

In this review, applications of both metal-free NCs and metal-supported NC catalysts for the ORR are reviewed; other materials reported for the ORR are beyond the scope of this review. For the ORR, two reaction pathways exist, dependent on the type of electrolyte and nature of the catalyst.[123] In the first pathway, the molecular oxygen is reduced by four electrons to water, while in the second pathway, which is less efficient, the molecular oxygen gets reduced by two electrons to produce a H_2O_2 intermediate. Sun *et al.* reported the electrochemical two-electron ORR *via* the H_2O_2 pathway using NC prepared by direct pyrolysis of polyethylenimine with mesoporous carbon.[129] The efficient electrocatalyst can perform the ORR *via* the four-electron pathway without forming peroxide, resulting in higher efficiency of the fuel cell. Since peroxide formation lowers the current efficiency and operating potential, it also harms fuel cell components by corrosion.

$$O_2 + H^+ + 4e^- \rightarrow 2H_2O \text{ (first pathway)}$$

$$O_2 + 2H^+ + 2e^- \rightarrow H_2O_2 \text{ (second pathway)}$$

$$H_2O_2 + 2H^+ + 2e^- \rightarrow 2H_2O$$

Recently, NCs have been extensively studied as catalysts for the ORR because the N present in various configurations improves the electron-donating ability of NCs owing to its higher ORR activity.[130,131] Furthermore, the synthesis of metal-free NC catalysts and non-precious metal-supported NC catalysts and their ORR applications have attracted significant attention. The N with one additional electron and higher electronegativity than carbon tends to accept electrons from carbons leading to a partial positive charge on the carbon, resulting in enhanced interaction with O_2 and its dissociation adsorption.[123] Many electrocatalysts have been developed using carbon nanotubes, graphene, and ordered mesoporous carbons. The use of a hierarchical porous structure is beneficial because of meso- and macropores, facilitating the transport of O_2 and H_2O. The microporosity supports hosting more electrocatalytically active sites. Yang *et al.* reported NHPC foam to use as an electrocatalyst, which exhibits higher activity for the ORR, oxygen evolution reaction (OER) and N reduction reaction (NRR).[132]

The synthesis of cobalt–N-doped mesoporous carbon containing a high N/C atomic ratio (0.22) was reported using vitamin B12 and a polyaniline–Fe (PANI–Fe) complex.[133] This inexpensive, active, and stable mesoporous non-precious metal (NPM) catalyst prepared from vitamin B12 and silica nanoparticles could be a suitable alternative to the expensive Pt/C noble metal catalyst used for the ORR. The NPM catalyst showed remarkable ORR activity (0.79 V half-wave potential, *ca.* 58 mV deviation from Pt/C) in acidic media owing to its abundant metal–N active sites, high BET specific surface area (572 $m^2\ g^{-1}$), and narrow distribution of mesopores with well-defined porous structures. The conventional methods reported for the synthesis of transition metal–N-doped carbon frameworks involve direct pyrolysis of a mixture of carbon, N, and transition metal precursors, which usually fails to control the porous structure resulting in limited exposure of active sites. Besides, the synthesis of a N-doped non-precious iron metal catalyst (Fe-NC) was reported using soybean biomass.[134] This catalyst was produced by co-pyrolysis with metallic Fe and a carbon support from soybean biomass. In the presence of Fe metal, the three-dimensional quaternary N structure changed to planar pyrrolic or pyridinic N species in the carbon matrix during pyrolysis. This catalyst exhibited superior performance for the ORR in an alkaline electrolyte. It indicates that the planar N species acts as an active center and thus improves the ORR performance.

Zhang *et al.* reported an efficient method for the ORR using lignosulfonate biomass-derived N and S co-doped porous carbons.[135] In this case, functionalized lignin acts as both dopant and carbon precursor for the direct production of N and S co-doped carbon. This metal-free catalyst offers high activity, outstanding durability, and excellent selectivity for the ORR. The morphology of the material was a honeycomb-like flake carbon sheet network with a large BET specific surface area (1165 $m^2\ g^{-1}$), while the presence of N and S was confirmed

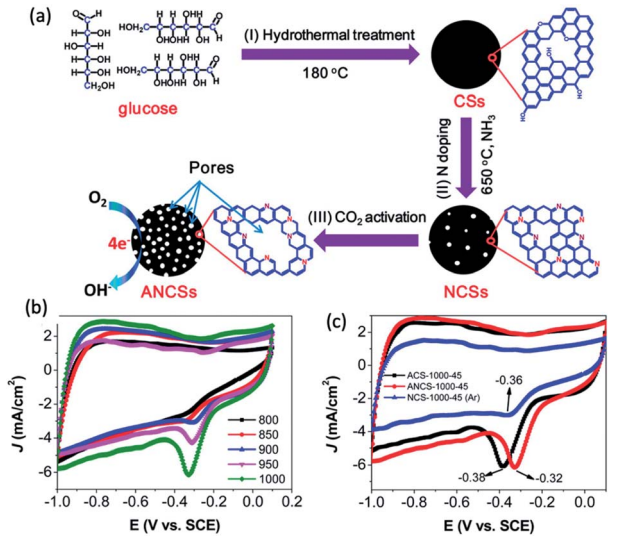

Fig. 13 (a) Schematic of highly porous ANCSs as efficient and stable ORR electrocatalysts *via* a multistep strategy. (b and c) CV curves of the activated samples (ANCSs), as well as the control samples in O_2-saturated 0.1 M KOH aqueous solution (sweep rate: 50 mV s^{-1}). Reproduced with permission from ref. [147], copyright (2017) ACS.

using XPS analysis. Thermal treatment was applied to control the dopant configuration and degree of graphitization.

Recently, for the ORR, the electrocatalytic properties of N and S co-doped carbons were reported.[135] Noticeably a high electrocatalytic response/cathodic current (*ca.* 0.72 V) was observed under O_2 compared to that under N_2 (Fig. 12(a)). The linear scan voltammogram (LSV) curve was obtained at various annealing temperatures for N-S/Cs, lignosulfonate (LS), and ammoniated lignosulfonate (ALS) under saturated O_2 (Fig. 12(b)). Compared to the ammoniated lignosulfonate and original lignosulfonate, the N and S co-doped catalysts showed high ORR onset potentials, indicating faster reaction kinetics with N and S co-doped catalysts (Fig. 12(c)). Moreover, the N and S co-doped catalyst prepared from lignin exhibited higher performance (0.80 V *vs.* RHE) compared to N-doped graphene (0.74 V *vs.* RHE),[136] N/S co-doped graphene,[137] N/S co-doped carbon nanofibers,[138] and carbon electrocatalysts.[139] The N-S/C_700 catalyst showed a high performance compared to 5% Pt/C in terms of current density and onset potential. Furthermore, it exhibited close limiting current density to that of a 20% Pt/C catalyst regardless of its smaller onset potential (0.80 V *vs.* RHE) relative to 20% Pt/C (0.95% V *vs.* RHE), as shown in Fig. 12(b). Current density and onset potential were tested at various potentials for each ORR with total N content.

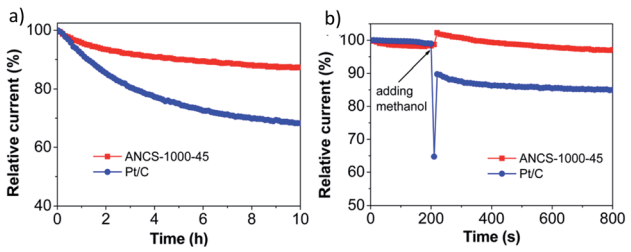

Fig. 14 (a) The chronoamperometric responses of ANCS-1000-45 and Pt/C at −0.6 V (*vs.* SCE) on an RDE at 1600 rpm, and (b) the chronoamperometric responses of ANCS-1000-45 and Pt/C at −0.6 V (*vs.* SCE) on an RDE at 1600 rpm in O_2-saturated 0.1 M KOH before (0–200 s) and after (200–800 s) adding 3 M methanol. Reproduced with permission from ref. 147, copyright (2017) ACS.

The catalyst with a higher graphitization degree showed superior current density. The graphitization improves electron transfer, which is beneficial for high ORR performance. Higher pyridinic and graphitic N contents were achieved with the N-S/C_700 catalyst showing superior ORR activity (Fig. 12(d and e)). Furthermore, the Koutecky–Levich (K–L) analysis showed a linear correlation between $1/w^{1/2}$ and $1/i$, as shown in Fig. 12(f). For N-S/C_700 and N-S/C_800, the K–L analysis results remained almost constant in the potential range of 0.3 to 0.6 V (Fig. 12(g)), higher than those of N- (3.2 at 0.75)[140] and S-doped graphene (3.2 at 0.477)[141] and other carbon catalysts.[139] These results indicated that the ORR catalyzed using N-S/C_700 proceeded mainly through a one-step four-electron process. High values of electron transfer were achieved for all N-S/C samples compared to the ammoniated lignosulfonate and original lignosulfonate (Fig. 12(g)). The high ORR activity of N-S/C_700 is seen from its smaller Tafel slope than those of other N-S/C samples in 0.1 M KOH, as shown in Fig. 12(h).

Many reports suggested that an increase in graphitic-N resulted in enhanced electrocatalytic activity. Conversely, the electrocatalytic activity was not significantly dependent on the pyridinic-N.[142,143] However, some reports showed that pyridinic-N and quaternary-N functionalities correlated with ORR activity instead of the total N content in the electrocatalyst. Additionally, many reports showed that graphitic-N was crucial for higher ORR activity.[128] Besides, both pyridinic-N and graphitic-N functionalities of NCs were also beneficial for the ORR activity.[144] The graphitic-N concentration determines the limiting current density, and the pyridinic-N concentration help to enhance the ORR onset potential. Recently, Sun *et al.* demonstrated that the pyridinic-N catalytic sites are active in acidic solution, while in alkaline and neutral solutions, graphitic-N catalytic sites are active for the ORR.[129] Zhao *et al.* reported that the ORR activity changes with quaternary-N and pyridinic-N concentration instead of the total N content.[145] However, NC nanotubes with low N content (0.56%) can also enhance the ORR activity.[123]

The 3D hierarchical NPC prepared using mixed cellulose ester film modified with polydopamine followed by KOH activation exhibited ORR activity similar to that of a Pt/C electrocatalyst.[146] The higher ORR activity is a result of the high specific surface area (2191 m^2 g^{-1}), which provides more catalytically active sites and has greater influence than pyridinic-N and pyrrolic-N functionalities. The exact role of various N functionalities and whether the content of N has an effect on the ORR are not clearly understood. Although plausible mechanisms have been proposed for the ORR using NCs as electrocatalysts, the mechanism of the ORR over NC is not explained precisely because of inadequate information about the nature of active sites and the use of different synthesis methods. The NCs

show higher activity compared to the commercial Pt/C catalyst in alkaline media. However, in acidic media lower activity was observed. The stability of the NCs is an issue in acidic solvent due to oxidation or protonation of N in an acidic environment. This problem can be partially solved using a higher degree of graphitic-N because the graphitic-N atoms are less prone to protonation. Besides, the use of a non-noble metal such as Fe or Co supported on NCs can also improve the activity in acidic media.

Gu *et al.* reported the synthesis of N-doped porous carbon spheres (NCSs) from biomass-derived glucose as a carbon source and N-doping by ammonia treatment with improved porosity for the ORR.[147] The carbon source was prepared by hydrothermal treatment using glucose as a substrate, as shown in Fig. 13(a). The carbon source was calcined at 650 °C under an ammonia flow to prepare NCS. The CO_2 activation was carried out by heating NCS at 800 to 1050 °C under a CO_2 flow for 0 to 90 min, as shown in Fig. 13(a). The electrocatalytic activity was investigated for the activated N-doped carbon sphere (ANCS) catalyst in a three-electrode system. The result showed superior conductivity with a high capacitive current. The oxygen reduction on the electrode surface is confirmed by the oxygen reduction peaks at −0.30 to −0.35 V (*vs.* reference electrode, *i.e.*, secondary calomel electrode) in the cyclic voltammetry (CV) curve. A significant increase in the ORR peak intensity was observed with the increase in activation temperature, indicating an enhanced electrocatalytic activity. The activated catalyst with N-doping showed a more positive ORR peak (−0.32 *vs.* saturated calomel electrode; SCE) compared to that without N-doping (−0.38 *vs.* SCE) and activation (−0.36 *vs.* SCE), as shown in Fig. 13(b). The increase in activation temperature led to improved ORR activity and higher limiting current density for a more positive onset potential. The thermal activation caused high ORR activity because of improved pore volume and surface area. The sample activated at 1000 °C for 45 min (ANCS-1000-45) exhibited high limiting current density (5.1 mA cm^{-2}) compared to previously reported NC electrocatalysts and even commercial Pt (4.2 mA cm^{-2}).[148,149]

The stability of the electrocatalyst during the ORR is the main challenge for practical fuel cell applications. The commercial Pt/C catalyst has inferior durability during long-term operation. Aggregation of Pt and its leaching from the carbon support, mentioned in some reports, results in a decrease in the ORR performance. The stability of commercial Pt/C and ANCS-1000-45 catalysts is tested in 0.1 M KOH solution under saturated O_2 and constant potential (−0.6 V *vs.* SCE), as presented in Fig. 14(a). The Pt/C catalyst showed a decrease in the current to 68% over the 10 h testing period, while the ANCS-1000-45 showed only a 13% decrease in current under similar conditions. This comparison result implies the excellent stability of the ANCS-1000-45 catalyst in 0.1 M KOH solution. In direct methanol fuel cells, the methanol crossover effect for the ORR electrocatalyst is a challenging problem for Pt-based catalysts. The ANCS-1000-45 and Pt/C catalysts were investigated for methanol oxidation by chronoamperometric measurements in 0.1 M KOH solution under saturated O_2 with 3 M methanol added at 200 s, as shown in Fig. 14(b). The results indicated that the ANCS-1000-45 catalyst showed stable cathodic ORR current after the addition of methanol in the cell. Conversely, a sharp decrease in current density was observed for the Pt/C catalyst under similar conditions, suggesting that the ANCS-1000-45 catalyst showed high selectivity and superior stability for the ORR and excellent tolerance to the methanol crossover effect.

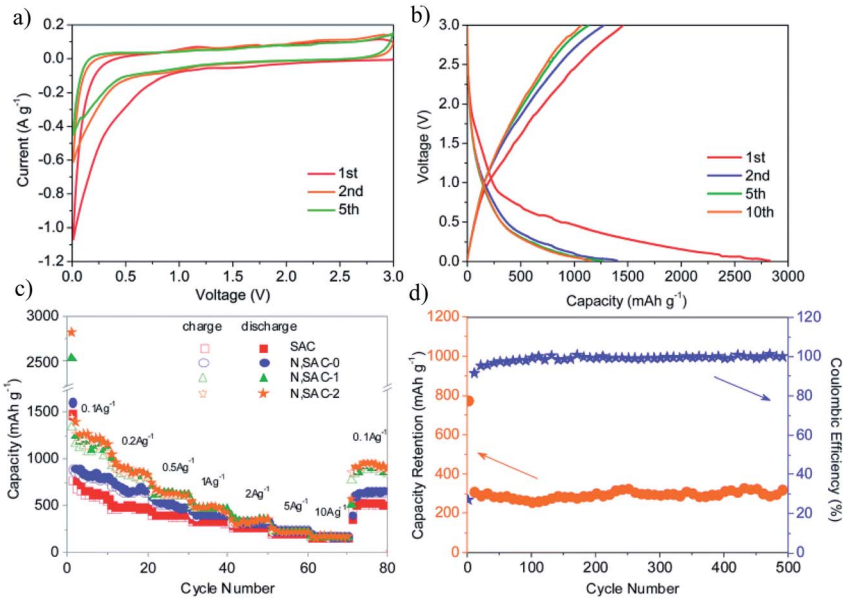

Fig. 15 (a) CV curves and (b) galvanostatic charge–discharge profiles for N,SAC-2. (c) Specific capacitances at different current densities. (d) The cycling test of the N,SAC-2 electrode at a current density of 2 A g^{-1} for 500 cycles. Reproduced with permission from ref. 156, copyright (2017) RSC.

3.2.2 Batteries. Currently, two major problems exist for the application of hydrogen fuel cells in vehicles; first, most of the industrial H_2 is obtained from methane (methane + oxygen = $2H_2 + CO_2$), which causes the greenhouse effect because of the formation of CO_2 during the process. The second issue is the storage and transportation of hydrogen. This difficulty makes the vehicles of the future more likely to be powered by batteries. Recently, NCs have been extensively used as potential anode materials in batteries to improve the electronic conductivity; the introduction of N provides active sites for Li-ion adsorption in Li-ion batteries.

The N content of N-doped graphene can considerably influence the Li-ion storage capacity.[150] Graphene and N-doped graphene have been reported as potential anode materials for Li-ion batteries due to their high surface area, superior mechanical flexibility, and excellent electronic and electrical properties. Besides N-doping, doping with other heteroatoms such as boron, phosphorus, and sulfur has been extensively studied for battery applications.[151] The results suggested that heteroatom doped carbons exhibited excellent cycling stability and higher specific capacities compared to non-doped carbon. The N-doped graphitic carbon promotes strong interaction between the Li-ions and the NC.[151] Low doping of N (3.9 atom%) can improve the Li storage capacity up to 600 mA h g^{-1}. The N-doped graphene nanosheets showed a superior reversible capacity of 900 mA h g^{-1} with high rate performance (250 mA h g^{-1}).[151,152] This demonstrates that N-doped graphene nanosheets are a promising anode material candidate for Li-ion batteries with high rate capability.[153,154]

The incorporation of N into carbon promotes Li storage by providing more active sites for Li storage. The higher specific surface area results in efficient contact between the electrode of NC and the electrolyte, which further facilitates the transportation of Li-ions.[155] The pores not only accommodate the local volume alteration of the carbon anode but also act as reservoirs for the storage of Li ions. The N-rich carbon derived from ox horn has hierarchical pores along with meso- and micropores affording easy transportation and storage of Li-ions. The micropores can act as charge accommodation sites, while the mesopores can shorten the length of Li-ion diffusion by forming an ion-buffering reservoir, and the interconnected pores offer a continuous electron transport route. The N-doping results in the formation of a large number of structural defects that promote rapid charge-transfer reactions and work as Li-insertion sites for Li-ion storage, which enhances the Li-ion storage performance.

The NPC prepared using natural polysaccharides such as sodium alginate and additional N precursor urea *via* KOH activation showed superior electrochemical performance for the Li-ion battery application.[156] This NC derived from the sodium alginate (NSAC-*n*, where *n* denotes the KOH to sodium alginate mass ratio) electrode exhibited a high specific capacity of 1455 mA h g^{-1} for Li-ion batteries. The performance of sodium alginate-derived NPC was examined in $LiPF_6$ electrolyte using coin-type half cells. The CV curves were recorded at a scan rate of 0.1 mV s^{-1} and voltage range 0.01 to 3 V, and are presented in Fig. 15(a). The cathodic peak was observed over the potential range from 0.01 to 1 and 0.01 to 0.5 in the first and following CV scans. In the first cycle, the electrode decomposition happens, which results in a pronounced peak in the initial cycle scan. The CV curves were similar to each other for the subsequent cycles, indicating the excellent electrochemical reversibility of the electrodes. The NSAC-0 sample exhibited higher reversible charge capacity (893 mA h g^{-1}) than carbon derived from sodium alginate (SAC 774 mA h g^{-1}) at 0.1 A g^{-1}, while higher charge capacity was achieved for NSAC-1 (1334 mA h g^{-1}) and

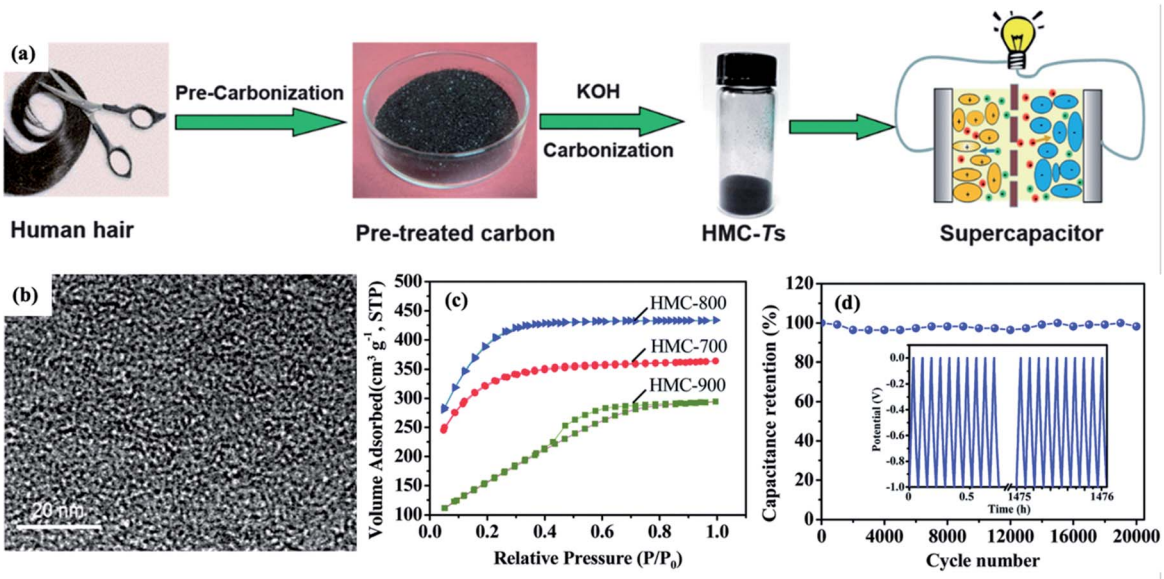

Fig. 16 (a) Fabrication of HMCs, (b) HR-TEM images of the HMCs obtained at 800 °C, (c) N sorption isotherms, (d) cycling stability of HMC-800 at a charge–discharge current density of 2 A g^{-1} for 20 000 cycles in 6 M KOH electrolyte. Inset: galvanostatic charge–discharge cycles. Reproduced with permission from ref. 79, copyright (2014) RSC.

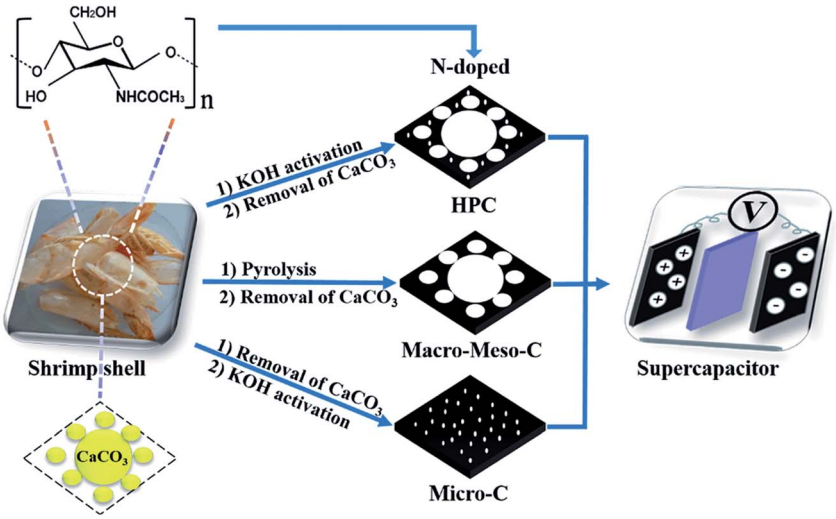

Fig. 17 Synthesis schematic of N-doped HPC, macro–meso-C, and micro-C from shrimp shell. Reproduced with permission from ref. 171, copyright (2016) RSC.

NSAC-2 (1455 mA h g^{-1}), due to the N-doping and a higher surface area, which contribute to the enhanced Li storage capacity.

The rate capability of NSAC was provided under various current densities from 0.1 to 10 A g^{-1}, as shown in Fig. 15(c). The rate capacity remained at 223 and 173 mA h g^{-1} for NSAC-2 for high current densities of 5 and 10 A g^{-1}. The higher surface area is favorable for enhancing the capacity, and the lower N content results in decreased capacity. The capacity and coulombic efficiency were maintained with no sign of decomposition for 500 cycles, suggesting that this NSAC electrode has potential for practical applications, as shown in Fig. 15(d). The high Li storage capacity, superior rate capability, and excellent cycling stability of the NSAC electrode showed that NSAC is a potential anode material for Li-ion batteries.

For high-performance Li-ion batteries, Mondal *et al.* synthesized NPC using shrimp shell waste.[157] The shrimp shell-derived NPC was used in a Li-ion battery as an anode material and showed a high specific capacity of 1507 mA h g^{-1} at 0.1 A g^{-1} current density. Recently, as an alternative to Li-ion batteries, Na-ion batteries were studied using NCs because of the low cost of Na metal and its abundance compared to Li.[158] The electrochemical activity of the Na-ion battery significantly depends on the electrode pore size and morphology because of the relatively larger size of the Na-ion compared to that of the Li-ion. The N-doping facilitates the diffusion of Na-ions because it helps to increase the defects and lattice spacing between two adjacent graphene sheets, which leads to a significant increase in the performance of Na-ion batteries. Li *et al.* reported red phosphorus confined in a N-doped microporous carbon matrix to improve Na storage performance.[159] The incorporation of red P enhanced the rate capacity by *ca.* 450 mA h g^{-1} after 1000 cycles. The red P can electrochemically react with Na forming Na_3P, consequently delivering high theoretical Na storage capacity (2595 mA h g^{-1}), while white P was not selected for the electrochemical application because of its high reactivity with air and flammability issues. Along with P, doping other heteroatoms, including boron,[160,161] sulfur,[162–164] and iodine,[165,166] has been studied for Na-ion batteries to enhance the energy storage performance.

3.2.3 Supercapacitors. Supercapacitors (SCs) are also called ultracapacitors or electrochemical capacitors. They can store electrical energy electrostatically/electrochemically in a polarizing electrolytic solution. SCs are classified into three types depending on the energy storage mechanism: (1) double-layer capacitors, which exhibit electrostatic charge storage (electrochemical double-layer capacitors (EDLCs)/Helmholtz layer mechanism), (2) pseudocapacitors, which exhibit electrochemical charge storage (redox reaction) and (3) hybrid capacitors, which exhibit electrostatic and electrochemical charge storage. For EDLCs, usually, active carbons are used as electrodes, and the energy storage mechanism is through adsorption/desorption on the interface of the electrode/electrolyte. On the other hand, in pseudocapacitors, metal oxides such as RuO_2, V_2O_5, MnO_2, and conducting polymers are used as electrodes, and the energy storage mechanism is

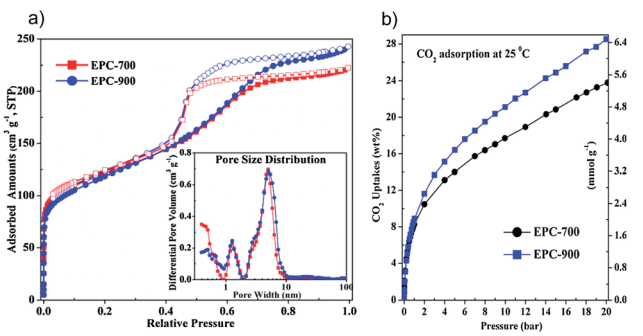

Fig. 18 (a) N_2 sorption isotherm (the pore size distribution is shown in the inset). (b) CO_2 adsorption isotherm at 25 °C. Reproduced with permission from ref. 174, copyright (2016) Elsevier.

through redox reactions. Pseudocapacitors offer higher specific capacitance and energy density compared to EDLCs. However, they suffer from a lack of stability because of framework swelling and modest electrical conductivity during cycling.[167] Although EDLCs have lower energy density than pseudocapacitors, EDLCs can work at high charge and discharge rates and have superior cycling stability. Hybrid SCs have benefits of EDLCs and pseudocapacitors. Therefore, charge storage happens electrostatically and electrochemically or through a combination of both.

Recently, for SCs, biomass-derived carbon and NCs have been widely used as electrode materials.[60] The specific capacitance of a carbon electrode was enhanced without sacrificing the long cycle life and high rate capability by doping various heteroatoms (N, O, P, S, and B).[168,169] Today, the major issue with SCs is their lower energy density (10 W h kg^{-1}) compared to Li-ion batteries (180 W h kg^{-1}). Therefore, enhancing the energy density of SCs by developing active electrodes and novel electrolytes that can work in a broad range of operational voltages has attracted significant attention.

Qian *et al.* reported superior charge storage capacity in 6 M KOH with a specific capacitance of 340 F g^{-1} at a current density of 1 A g^{-1} for human hair-derived micro/mesoporous carbon (HMC), as shown in Fig. 16.[79] The activation temperature significantly affects the porosity of the material (Fig. 16(c)); an increased activation temperature from 700 to 800 °C leads to an increase in surface area and pore volume. The narrow pore size distribution and higher surface area are useful in charge storage. The HMC-900 showed both micropore and mesopore formation, indicated by the hysteresis loop from $P/P_0 = 0.4$ to 0.8. The HMC-900 catalyst exhibited excellent stability; the long-term activity maintained *ca.* 98% of the starting specific capacitance over 20 000 cycles in 6 M KOH (Fig. 16(d)).

The low-cost shrimp shell is a reliable N-containing polysaccharide obtained from food waste. The natural inorganic $CaCO_3$ composition of the shrimp shell can serve as a carbon template for NC synthesis. White *et al.* initially used shrimp shell (prawn shell) to fabricate an NPC with high surface area, mesoporosity, and high N content in a three simple step synthetic approach.[170] Gao *et al.* reported using waste shrimp shells as the precursor for the synthesis of N-doped HPC by a self-templating route combined with KOH activation.[171] The KOH activation produces micropores in the carbon. In this case, the shrimp shell was activated by KOH at 600 to 800 °C under an Ar atmosphere to yield micropores; then macro- and micropores were formed by removing the $CaCO_3$ template using acetic acid, as shown in Fig. 17. Changing the activation temperature without N loss can tailor the specific surface area of the as-synthesized N-doped HPC. The obtained N-doped HPC with abundant micro-, meso-, and interconnected macropores was an excellent electrode material for SCs. The HPC exhibited a high capacitance of 348 F g^{-1} in 6 M KOH electrolyte due to the synergistic effect of electrochemical activity arising from porosity and heteroatoms. The same group further adopted this concept to synthesize NPC as a cathode material for Li–S batteries. Among the different porous structures, a mesoporous carbon cathode possessed a large pore size (5.12 nm) and high N content (6.67 wt%), and exhibited cycling stability with 90% retention within 100 cycles.[172]

Shao *et al.* applied cattle bone-derived meso- and macroporous NHPCs for high energy and ultrafast SCs in organic and IL electrolytes.[173] The NHPCs obtained have dominant meso- and macroporosity with a high specific area of 2203 m^2 g^{-1} due to the KOH activation and hydroxyapatite in the cattle bone. This cattle bone-derived NHPC electrocatalyst showed excellent capacitive performance in 1.0 M $EMIMBF_4$ IL electrolyte (240 F g^{-1} at 5 A g^{-1}). Ferrero *et al.* used soybean with high N content as a biomass precursor for SCs. The HTC of the defatted soybean solid residue produces NPCs.[75] First, commercial soya flour was defatted by Soxhlet extraction. Then, the defatted soybean solid residue was mixed with glucose and charged into a stainless-steel autoclave for HTC. The resulting solid (hydro char) was further activated by KOH, followed by the second carbonization. Subsequently, the N-doped microporous carbon

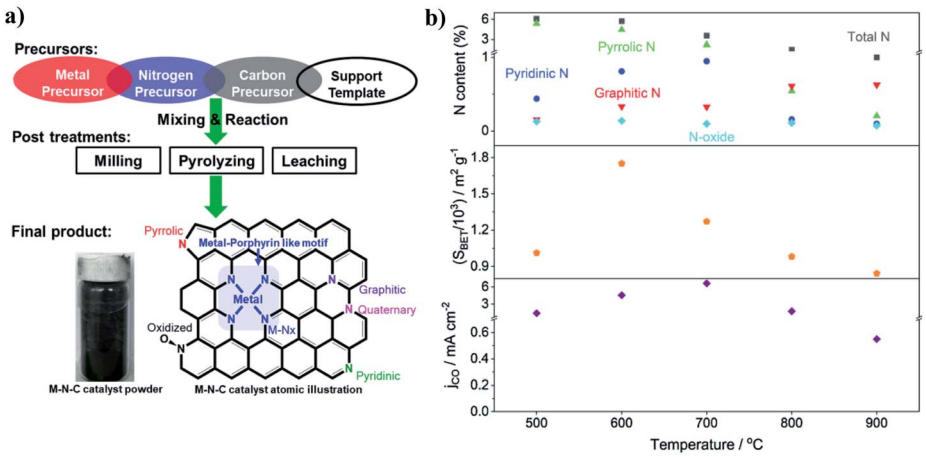

Fig. 19 (a) Typical synthesis strategy of metal-NC catalysts and their resulting structure. Reproduced with permission from ref. 180, copyright (2019) ACS. (b) The partial current density of CO on NC synthesized at various temperatures as a function of surface areas and nitrogen content. Reproduced with permission from ref. 185, copyright (2017) Elsevier.

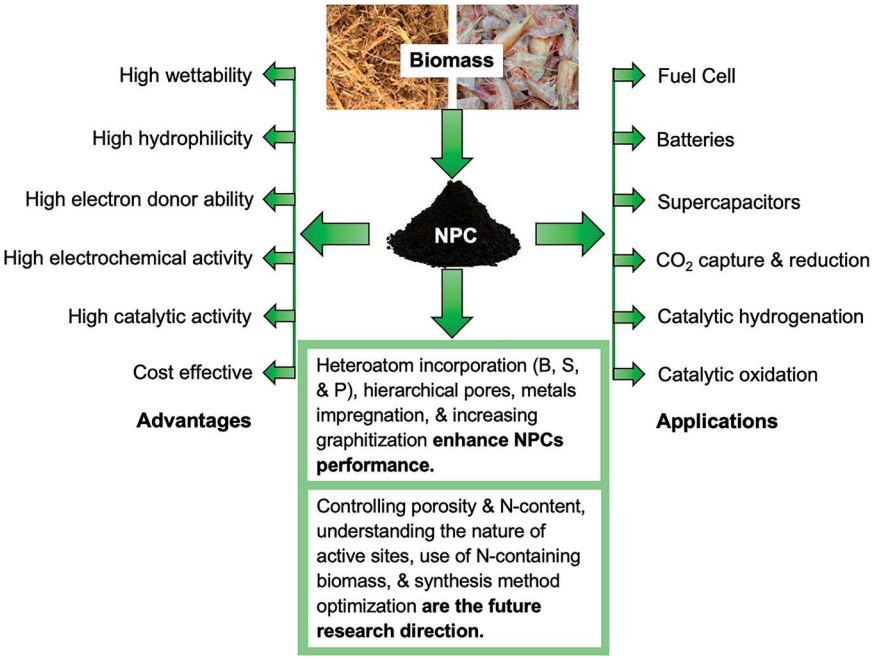

Fig. 20 Conclusion and outlook summary.

can be obtained for the SC application, as shown in Fig. 8(a). The SEM analysis suggests that the activated samples have an irregular morphology with huge conchoidal cavities, which can promote easy access to the inner pore structure.

This N-doped microporous carbon exhibited high capacitive performance in volumetric and gravimetric units when employed as SCs in aqueous electrolyte (Li_2SO_4 and H_2SO_4). In Li_2SO_4, the voltage window extended up to 1.7 V, while in H_2SO_4, it extended to 1.1 V, indicating that the energy stored is increased by 50% compared to that in the H_2SO_4 electrolyte. The results showed a pseudo-capacitance phenomenon contributed by the oxygen and N functionalities. The NC synthesized at a lower temperature (600 °C) is suitable for SCs with lower discharge rates (less than 5 A g^{-1}), while the NC prepared at a higher temperature (800 °C) is more appropriate for higher rates. The NC synthesized from waste shrimp shells showed superior performance in Li-ion batteries and SCs due to the presence of heteroatoms and a unique porous structure.[157]

3.3 CO_2 capture and reduction

Aside from the applications of NPCs in the ORR, rechargeable batteries and SCs, biomass-derived NPCs were used in CO_2 capture as multi-functional materials. Tian *et al.* recycled algae pollutants of *Enteromorpha prolifera* (EP) to obtain N and O co-doped hierarchical carbon through direct carbonization of freeze-drying treated algae.[174] This heteroatom doped hierarchical carbon showed excellent performance for CO_2 capture and SCs. The N and O co-doped hierarchical carbon pyrolyzed at 900 °C showed 2.0 and 6.5 mmol g^{-1} CO_2 uptakes under 2 MPa at 25 °C.

The EP-derived N and O co-doped hierarchical carbon obtained at 700 and 900 °C pyrolysis temperatures (EPC-700 and EPC-900) showed type IV isotherms, as shown in Fig. 18(a). The hysteresis loop was realized in the pressure range of 0.45 to 1, suggesting that the material is mesoporous. The presence of micropores was indicated by the adsorption of a large quantity of N_2 molecules below a relative pressure of 0.05. The EPCs are excellent for SC applications because of hierarchical pores at 1.5 to 5 nm and micropores (Fig. 18(a)). Typically, the CO_2 adsorption increases with an increased pore volume and surface area under high pressure. Although EPC-700 and EPC-900 have similar pore size distributions and N_2 adsorption isotherms, the total micro-porosity of EPC-700 was slightly higher than that of EPC-900. The EPC-900 exhibited higher CO_2 capture at 2 MPa pressure than EPC-700, as shown in Fig. 18(b). The CO_2 uptake with EPC-900 at 1 MPa was still higher (2.01 mmol g^{-1}) than that with the microporous carbon sphere from the silica template (1.1 mmol g^{-1}), which has a surface area of 463 m^2 g^{-1}.[175]

Notably, Rana *et al.* synthesized NC with high surface area (1072 m^2 g^{-1}) from soya for tri-functional applications (ORR, SCs, and CO_2 capture).[76] This soya-derived NC was synthesized by carbonization with three easy steps: (1) soya chunks were milled and heated at 300 °C (3 h) in an inert atmosphere; (2) the carbonized sample was activated by NaOH at 600 °C (1 h) in an inert atmosphere and further neutralized by HCl; (3) the obtained activated carbon was then pyrolyzed at 800, 900, and 1000 °C in an inert atmosphere for an additional 2 h, as shown in Fig. 8(b). The soya derived NC exhibited excellent performance in the ORR, SCs, and CO_2 capture due to the presence of heteroatoms and their chemical nature. For the ORR, increasing the annealing temperature from 900 to 1000 °C could not only promote the coexistence of graphitic and pyridinic-N but could also enhance the conductivity of the sample, which

were beneficial for the ORR activity. The pyridinic-N sites with Lewis basicity also have the ability for CO_2 stabilization and adsorption. In addition to the ORR and CO_2 adsorption, oxygen in the material also contributes to the supercapacitive properties. Therefore, this soya derived NC exhibited superior performance for ORR, CO_2 capture, and SC applications, as shown in Fig. 8(b).

The electrochemical CO_2 reduction reaction (CO_2RR) is one of the beneficial approaches compared to other types of CO_2 conversion methods because of its several advantages. The electrochemical CO_2 conversion into fuels and chemicals was performed under ambient pressure and moderate reaction temperature.[176] Moreover, electricity helped to drive the CO_2RR. However, CO_2 reduction with lower operating overpotential and high product selectivity under mild reaction conditions is challenging.[176–178]

Recently, for CO_2 reduction, Yao *et al.* reported highly efficient N-doped nanoporous carbon from Typha biomass.[179] The result showed high CO selectivity (90%) at a lower overpotential (−0.31 V). The pyridine species of NC plays a crucial role in catalytic activity; the kind of N species and the porous structure were significantly affected by calcination temperature. The electrocatalytic CO_2 reduction was greatly enhanced by incorporating S atoms in the NCs.[177] The result indicates that the incorporation of S induces highly dense pyridinic N species, which has highly active sites for CO_2 reduction. Furthermore, it enhances the intrinsic catalytic reactivity of graphitic N and pyridinic N by decreasing the energy barrier for the generation of the *COOH intermediate. High CO faradaic efficiency (92%) and CO current (2.63 mA cm^{-2}) were achieved at a lower overpotential (490 mV) using N,S-codoped carbon; this is a superior result compared to NC without S incorporation. Besides, the encapsulation of Ni nanoparticles into NC led to enhanced catalytic activity for the efficient reduction of CO_2 into CO with excellent stability.[176] The incorporation of Ni nanoparticles helps to decrease the activation barriers of NC catalysts for tuning the local electron distribution of the surface reaction.

NC containing transition metals were reported as cost-effective catalysts by Varela *et al.* to reduce CO_2 into CO.[180] The transition metal and NCs offer high selectivity for the CO_2 reduction into CO at low overpotential; the partial current density of CO in the aqueous electrolyte is 223 mA cm^{-2}. Transition metal-NCs are a low-cost alternative to the Pt in fuel cell electrodes because of their higher activity for the ORR.[181] The metal can coordinate with various N species to form catalytically active single-sites similar to molecular metal N-macrocycles, as shown in Fig. 19(a).[182–184] Li *et al.* reported the electrocatalytic CO_2 reduction over NPC synthesized using pyrolysis of wheat flour biomass. The result showed 83.7% faradaic efficiency for CO_2 reduction into CO at a 0.71 V overpotential in aqueous media. This NC exhibited long-term durability, and mechanistic studies have indicated that pyridine N-species promote high catalytic activity. The active sites for the CO_2RR and CO formation are pyridinic N defects (Fig. 19(b)). The surface area is not entirely consistent with the performance of the catalyst. The graphitic N is less accessible for CO_2 binding because, in graphitic N, the electrons are present in the π^* antibonding orbital.

Besides the CO_2RR, CO_2 incorporation into carbonates and other chemicals such as acrylic acid and urea is also a promising approach for the utilization of CO_2 to decrease carbon emissions. Recently, Kamphuis *et al.* presented a review on the applications of CO_2 incorporation into cyclic and polymeric carbonates.[186]

4. Conclusions and outlook

In this review, we reviewed various synthesis methods for NPCs. The synthesis methods of NPCs had a notable impact on their physicochemical properties. The applications of NPCs and metal-supported NPCs for energy storage applications, including fuel cells, batteries, SCs, and CO_2 reduction, are discussed. Furthermore, NPC catalysts showed high activity in hydrogenation reactions and the oxidation of biomass-derived HMF and furfural. The utilization of NPC has many advantages over porous carbon. For example, the incorporation of N increases wettability and hydrophilicity. N has a higher electronegativity than carbon; hence, N-doping can enhance the electron donating ability of the NCs and the electrochemical activity. The use of a variety of N-containing biomass such as shrimp shells, algae, soybean waste, and chitosan for the synthesis of NPCs can avoid the use of additional nitrogen precursors. Some biomass contains templates such as SiO_2 in rice husk, MOF in *Enteromorpha prolifera*, and $CaCO_3$ in soft pitch, which act as self-templates. It enhances the specific surface area while converting biomass into NPCs. The synthesis of a 3D N-doped framework typically performed *via* the calcination of biomass is a cost-effective approach. NPCs are broadly produced using HTC and pyrolysis methods. Along with N-doping, incorporating other heteroatoms (B, S, and P) in the carbon framework sometimes enhances the catalyst activity/electrochemical performance, so future attempts on the synthesis of heteroatom co-doped carbons should be focused on using biomass. Besides, with heteroatom incorporation, the surface properties of the NCs improved by forming hierarchical pores.

NPCs have been used extensively as electrode materials for various batteries. The pyrrolic and pyridinic N atoms promote Li storage, and these N species exhibited strong interaction with Li-ions. Similarly, quaternary and pyridinic N atoms offer active sites for the ORR in metal–air batteries. However, the working mechanism of these active sites is not well understood. Hence, the mechanistic study of these reactions is an essential topic for the development of efficient, cost-effective NCs as promising electrode materials for advanced battery applications. Selection of renewable biomass-derived carbon sources, including cellulose, lignin, and crop wastes, should be encouraged for the synthesis of NC to decrease the dependence on fossil feedstock. Besides, for NPC synthesis, the use of chitin, shrimp shells, and algae needs to be focused on. It is challenging to successfully tune the ratio of N types and the N-content for a specific application. Furthermore, the stability of NCs is an issue in acidic media due to the protonation or oxidation of N in an

acidic environment. The use of NCs with a high degree of graphitization can solve this issue because the graphitic-N atoms are less prone to protonation.

The use of a non-noble metal such as Fe or Co supported on NCs can enhance the activity in acidic media. Although metal-based NCs have shown high catalytic activity, they suffer from metal leaching, reutilization and separation issues, and toxic waste production, which makes them unattractive for an environmentally benign sustainable process. The optimization of preparation methods for metal-free NCs and the promotion of their applications can solve this problem. The pore diameter of biomass-based NC electrodes has a significant effect on their electrochemical properties. The porosity is closely related to the electron transfer, and it is an essential factor in determining the rate capability and specific capacitance. However, controlling the pore structure and size of biomass-derived NCs is challenging. Therefore, the optimization of controlling the pore structure by tuning the synthesis methods and selecting suitable biomass is highly desirable for further activity improvement.

We envisaged that for a series of emerging applications in the areas of rapid charge-storage and efficient charge–discharge profiles of potassium-ion batteries and lithium–oxygen batteries, respectively, NPCs of specific geometry are desired since electrodes with maximized atomic exposed sites are essential for tailoring the formation/decomposition of nano-sized lithium peroxide during the ORR with greatly enhanced redox kinetics and overpotentials. In such a process, NCs in nanosheet geometry for metal atom dispersion are ideal,[187] and therefore, strategies for obtaining nanosheet NCs from biomass resources will be desired future prospects. Another such kind of NC nanofiber offers enhanced rate capability and cyclability in charge storage batteries.[188] Additional strategies can be imagined for creating a metal-N_x active site where a confined metal can provide a superior activity for electrochemical processes.[189]

Future research needs to be focused on understanding the nature of active sites and gaining mechanistic insight into the ORR over NCs. The higher surface area of these NC electrocatalysts typically leads to superior activity if the external surface/active sites are accessible. Besides, the type of N species, degree of graphitization, and N content affects the conductivity and stability of the electrocatalysts. The use of higher pyrolysis temperature leads to a decrease in N content; consequently, optimum pyrolysis temperature is preferred to obtain a higher N content, which positively affects ORR activity. Moreover, to use these NCs as electrocatalysts on an industrial scale in an alkaline environment, development of suitable anion exchange membranes is required with high hydroxide conductivity and improved mechanical, thermal, and chemical stability. A summary of the conclusion and outlook is shown in Fig. 20 for visual representation. The future development of NC as an electrocatalyst for the ORR can help to commercialize fuel cell technology. Recent understanding of the exceptional properties and features of NCs and their versatile applications in catalysis and electrochemical energy storage can provide outstanding future direction in promoting sustainable chemistry.

Conflicts of interest

There are no conflicts to declare.

Acknowledgements

B. M. Matsagar acknowledges the Ministry of Science and Technology (MOST), Taiwan, for research funding (108-2638-E-002-003-MY2). This research was supported by the Hydrogen Energy Innovation Technology Development Program of the National Research Foundation of Korea (NRF) funded by the Korean government (Ministry of Science and ICT (MSIT)) (No. NRF-2019M3E6A1064197).

References

1 T. Lu, X. Xu, S. Zhang, L. Pan, Y. Wang, S. M. Alshehri, T. Ahamad, M. Kim, J. Na, M. S. A. Hossain, J. G. Shapter and Y. Yamauchi, *Bull. Chem. Soc. Jpn.*, 2020, **93**, 1014–1019.
2 H. Qi, M. Teng, M. Liu, S. Liu, J. Li, H. Yu, C. Teng, Z. Huang, H. Liu, Q. Shao, A. Umar, T. Ding, Q. Gao and Z. Guo, *J. Colloid Interface Sci.*, 2019, **539**, 332–341.
3 X. Zhou, P. L. Wang, Y. G. Zhang, L. L. Wang, L. T. Zhang, L. Zhang, L. Xu and L. Liu, *J. Mater. Chem. A*, 2017, **5**, 12958–12968.
4 S. Gao, X. Li, L. Li and X. Wei, *Nano Energy*, 2017, **33**, 334–342.
5 N. Mohamad Nor, L. C. Lau, K. T. Lee and A. R. Mohamed, *J. Environ. Chem. Eng.*, 2013, **1**, 658–666.
6 S. De, A. M. Balu, J. C. Van Der Waal and R. Luque, *ChemCatChem*, 2015, **7**, 1608–1629.
7 J. H. Khan, J. Lin, C. Young, B. M. Matsagar, K. C. W. Wu, P. L. Dhepe, M. T. Islam, M. M. Rahman, L. K. Shrestha, S. M. Alshehri, T. Ahamad, R. R. Salunkhe, N. A. Kumar, D. J. Martin, Y. Yamauchi and M. S. A. Hossain, *Mater. Chem. Phys.*, 2018, **216**, 491–495.
8 Y.-T. Liao, B. M. Matsagar and K. C. W. Wu, *ACS Sustainable Chem. Eng.*, 2018, **6**, 13628–13643.
9 B. M. Matsagar, S. A. Hossain, T. Islam, H. R. Alamri, Z. A. Alothman, Y. Yamauchi, P. L. Dhepe and K. C. W. Wu, *Sci. Rep.*, 2017, **7**, 13508.
10 B. M. Matsagar and P. L. Dhepe, *New J. Chem.*, 2017, **41**, 6137–6144.
11 J. Niu, R. Shao, M. Liu, Y. Zan, M. Dou, J. Liu, Z. Zhang, Y. Huang and F. Wang, *Adv. Funct. Mater.*, 2019, **29**, 1905095.
12 F. Barzegar, A. Bello, D. Momodu, M. J. Madito, J. Dangbegnon and N. Manyala, *J. Power Sources*, 2016, **309**, 245–253.
13 Y. Lei, M. Gan, L. Ma, M. Jin, X. Zhang, G. Fu, P. Yang and M. Yan, *Ceram. Int.*, 2017, **43**, 6502–6510.
14 W. M. Qiao, S. H. Yoon and I. Mochida, *Energy Fuels*, 2006, **20**, 1680–1684.
15 Y. L. Wang, H. Q. Xuan, G. X. Lin, F. Wang, Z. Chen and X. P. Dong, *J. Power Sources*, 2016, **319**, 262–270.
16 T. Y. Wei, X. L. Wei, Y. Gao and H. M. Li, *Electrochim. Acta*, 2015, **169**, 186–194.

17 B. M. Matsagar, T. C. Kang, Z. Y. Wang, T. Yoshikawa, Y. Nakasaka, T. Masuda, L. C. Chuang and K. C. W. Wu, *React. Chem. Eng.*, 2019, **4**, 618–626.
18 Z. Bi, Q. Kong, Y. Cao, G. Sun, F. Su, X. Wei, X. Li, A. Ahmad, L. Xie and C.-M. Chen, *J. Mater. Chem. A*, 2019, **7**, 16028–16045.
19 J. Niu, J. Guan, M. Dou, Z. Zhang, J. Kong and F. Wang, *ACS Appl. Energy Mater.*, 2020, **3**, 2478–2489.
20 L. Yan, J. Yu, J. Houston, N. Flores and H. Luo, *Green Energy Environ.*, 2017, **2**, 84–99.
21 H. Watanabe, S. Asano, S.-I. Fujita, H. Yoshida and M. Arai, *ACS Catal.*, 2015, **5**, 2886–2894.
22 Q. Lv, W. Si, J. He, L. Sun, C. Zhang, N. Wang, Z. Yang, X. Li, X. Wang, W. Deng, Y. Long, C. Huang and Y. Li, *Nat. Commun.*, 2018, **9**, 3376.
23 D. Guo, R. Shibuya, C. Akiba, S. Saji, T. Kondo and J. Nakamura, *Science*, 2016, **351**, 361.
24 K. Sakaushi, A. Lyalin, S. Tominaka, T. Taketsugu and K. Uosaki, *ACS Nano*, 2017, **11**, 1770–1779.
25 J. Wu, Z. Pan, Y. Zhang, B. Wang and H. Peng, *J. Mater. Chem. A*, 2018, **6**, 12932–12944.
26 C. Wang, D. Wu, H. Wang, Z. Gao, F. Xu and K. Jiang, *J. Colloid Interface Sci.*, 2018, **523**, 133–143.
27 C. J. Wang, D. P. Wu, H. J. Wang, Z. Y. Gao, F. Xu and K. Jiang, *J. Power Sources*, 2017, **363**, 375–383.
28 L. Zhao, N. Baccile, S. Gross, Y. J. Zhang, W. Wei, Y. H. Sun, M. Antonietti and M. M. Titirici, *Carbon*, 2010, **48**, 3778–3787.
29 Y. S. Ren, Z. L. Yuan, K. L. Lv, J. Sun, Z. H. Zhang and Q. Chi, *Green Chem.*, 2018, **20**, 4946–4956.
30 J. Deng, M. Li and Y. Wang, *Green Chem.*, 2016, **18**, 4824–4854.
31 J. Huang, B. Zhao, T. Liu, J. Mou, Z. Jiang, J. Liu, H. Li and M. Liu, *Adv. Funct. Mater.*, 2019, **29**, 1902255.
32 K. Zou, Z. Guan, Y. Deng and G. Chen, *Carbon*, 2020, **161**, 25–35.
33 M. M. Titirici, R. J. White, C. Falco and M. Sevilla, *Energy Environ. Sci.*, 2012, **5**, 6796–6822.
34 J. Niu, R. Shao, M. Liu, J. Liang, Z. Zhang, M. Dou, Y. Huang and F. Wang, *Energy Storage Mater.*, 2018, **12**, 145–152.
35 N. Baccile, M. Antonietti and M. M. Titirici, *ChemSusChem*, 2010, **3**, 246–253.
36 M. M. Titirici, R. J. White, N. Brun, V. L. Budarin, D. S. Su, F. Del Monte, J. H. Clark and M. J. MacLachlan, *Chem. Soc. Rev.*, 2015, **44**, 250–290.
37 X. Sun and Y. Li, *Angew. Chem., Int. Ed.*, 2004, **43**, 597–601.
38 X. Fan, C. Yu, J. Yang, Z. Ling and J. Qiu, *Carbon*, 2014, **70**, 130–141.
39 L. Yu, C. Falco, J. Weber, R. J. White, J. Y. Howe and M.-M. Titirici, *Langmuir*, 2012, **28**, 12373–12383.
40 M. Sevilla and A. B. Fuertes, *Mater. Chem. Phys.*, 2009, **113**, 208–214.
41 M. Heidari, A. Dutta, B. Acharya and S. Mahmud, *J. Energy Inst.*, 2019, **92**, 1779–1799.
42 Y. Matsumura, in *Recent Advances in Thermo-Chemical Conversion of Biomass*, eds. A. Pandey, T. Bhaskar, M. Stöcker and R. K. Sukumaran, Elsevier, Boston, 2015, DOI: 10.1016/b978-0-444-63289-0.00009-0, pp. 251–267.
43 Z. Ling, C. Yu, X. Fan, S. Liu, J. Yang, M. Zhang, G. Wang, N. Xiao and J. Qiu, *Nanotechnology*, 2015, **26**, 374003.
44 B. M. Matsagar and P. L. Dhepe, *Catal. Sci. Technol.*, 2015, **5**, 531–539.
45 B. M. Matsagar, M. K. Munshi, A. A. Kelkar and P. L. Dhepe, *Catal. Sci. Technol.*, 2015, **5**, 5086–5090.
46 M. M. Titirici and M. Antonietti, *Chem. Soc. Rev.*, 2010, **39**, 103–116.
47 X. Cui, M. Antonietti and S. H. Yu, *Small*, 2006, **2**, 756–759.
48 G. Yu, B. Sun, Y. Pei, S. Xie, S. Yan, M. Qiao, K. Fan, X. Zhang and B. Zong, *J. Am. Chem. Soc.*, 2010, **132**, 935–937.
49 P. Chen, L. K. Wang, G. Wang, M. R. Gao, J. Ge, W. J. Yuan, Y. H. Shen, A. J. Xie and S. H. Yu, *Energy Environ. Sci.*, 2014, **7**, 4095–4103.
50 D.-W. Lee, M.-H. Jin, J.-H. Park, Y.-J. Lee and Y.-C. Choi, *ACS Sustainable Chem. Eng.*, 2018, **6**, 10454–10462.
51 V. Subramanian, C. Luo, A. M. Stephan, K. S. Nahm, S. Thomas and B. Q. Wei, *J. Phys. Chem. C*, 2007, **111**, 7527–7531.
52 M. Sevilla and R. Mokaya, *Energy Environ. Sci.*, 2014, **7**, 1250–1280.
53 P. Yang, J. W. Zhang, D. Liu, M. J. Liu, H. Zhang, P. S. Zhao and C. H. Zhang, *Microporous Mesoporous Mater.*, 2018, **266**, 198–203.
54 F. Liu, Z. Wang, H. Zhang, L. Jin, X. Chu, B. Gu, H. Huang and W. Yang, *Carbon*, 2019, **149**, 105–116.
55 W. Liu, J. Mei, G. Liu, Q. Kou, T. Yi and S. Xiao, *ACS Sustainable Chem. Eng.*, 2018, **6**, 11595–11605.
56 X. Tian, S. Zhu, J. Peng, Y. T. Zuo, G. Wang, X. H. Guo, N. Q. Zhao, Y. Q. Ma and L. Ma, *Electrochim. Acta*, 2017, **241**, 170–178.
57 W. Liu, G. Liu, Q. Kou and S. Xiao, *RSC Adv.*, 2017, **7**, 33875–33882.
58 L. T. Song, Z. Y. Wu, H. W. Liang, F. Zhou, Z. Y. Yu, L. Xu, Z. Pan and S. H. Yu, *Nano Energy*, 2016, **19**, 117–127.
59 R. Liu, H. Zhang, S. Liu, X. Zhang, T. Wu, X. Ge, Y. Zang, H. Zhao and G. Wang, *Phys. Chem. Chem. Phys.*, 2016, **18**, 4095–4101.
60 H. Lu and X. S. Zhao, *Sustainable Energy Fuels*, 2017, **1**, 1265–1281.
61 D. Lozano-Castelló, J. M. Calo, D. Cazorla-Amorós and A. Linares-Solano, *Carbon*, 2007, **45**, 2529–2536.
62 X. Fan, L. Zhang, G. Zhang, Z. Shu and J. Shi, *Carbon*, 2013, **61**, 423–430.
63 J. C. Wang and S. Kaskel, *J. Mater. Chem.*, 2012, **22**, 23710–23725.
64 M. Molina-Sabio and F. Rodríguez-Reinoso, *Colloids Surf., A*, 2004, **241**, 15–25.
65 C. Guan, K. Wang, C. Yang and X. S. Zhao, *Microporous Mesoporous Mater.*, 2009, **118**, 503–507.
66 M. J. Bleda-Martínez, J. A. Maciá-Agulló, D. Lozano-Castelló, E. Morallón, D. Cazorla-Amorós and A. Linares-Solano, *Carbon*, 2005, **43**, 2677–2684.
67 A. S. Marriott, A. J. Hunt, E. Bergström, J. Thomas-Oates and J. H. Clark, *J. Anal. Appl. Pyrolysis*, 2016, **121**, 62–66.

68 W. Suliman, J. B. Harsh, N. I. Abu-Lail, A. M. Fortuna, I. Dallmeyer and M. Garcia-Perez, *Biomass Bioenergy*, 2016, **84**, 37–48.
69 F. Suárez-García, A. Martínez-Alonso and J. M. D. Tascón, *J. Anal. Appl. Pyrolysis*, 2002, **63**, 283–301.
70 P. M. Eletskii, V. A. Yakovlev, V. B. Fenelonov and V. N. Parmon, *Kinet. Catal.*, 2008, **49**, 708–719.
71 M. Sevilla, A. B. Fuertes and R. Mokaya, *Energy Environ. Sci.*, 2011, **4**, 1400–1410.
72 J. C. Moreno-Piraján and L. Giraldo, *J. Anal. Appl. Pyrolysis*, 2010, **87**, 288–290.
73 T.-H. Liou, *Chem. Eng. J.*, 2010, **158**, 129–142.
74 R. Yavuz, H. Akyildiz, N. Karatepe and E. Cetinkaya, *Fuel Process. Technol.*, 2010, **91**, 80–87.
75 G. A. Ferrero, A. B. Fuertes and M. Sevilla, *Sci. Rep.*, 2015, **5**, 16618.
76 M. Rana, K. Subramani, M. Sathish and U. K. Gautam, *Carbon*, 2017, **114**, 679–689.
77 Z. Li, L. Zhang, B. S. Amirkhiz, X. Tan, Z. Xu, H. Wang, B. C. Olsen, C. M. B. Holt and D. Mitlin, *Adv. Energy Mater.*, 2012, **2**, 431–437.
78 X.-F. Li, Q. Xu, Y. Fu and Q.-X. Guo, *Environ. Prog. Sustainable Energy*, 2014, **33**, 519–526.
79 W. J. Qian, F. X. Sun, Y. H. Xu, L. H. Qiu, C. H. Liu, S. D. Wang and F. Yan, *Energy Environ. Sci.*, 2014, **7**, 379–386.
80 C. Schneidermann, C. Kensy, P. Otto, S. Oswald, L. Giebeler, D. Leistenschneider, S. Grätz, S. Dörfler, S. Kaskel and L. Borchardt, *ChemSusChem*, 2019, **12**, 310–319.
81 J. Liu, Y. Deng, X. Li and L. Wang, *ACS Sustainable Chem. Eng.*, 2016, **4**, 177–187.
82 G. Ma, Q. Yang, K. Sun, H. Peng, F. Ran, X. Zhao and Z. Lei, *Bioresour. Technol.*, 2015, **197**, 137–142.
83 Y. Zhang, L. Lu, S. Zhang, Z. Lv, D. Yang, J. Liu, Y. Chen, X. Tian, H. Jin and W. Song, *J. Mater. Chem. A*, 2018, **6**, 5740–5745.
84 B. Wang, S. Li, X. Wu, J. Liu and J. Chen, *J. Mater. Chem. A*, 2016, **4**, 11789–11799.
85 J. Zhao, Y. Liu, X. Quan, S. Chen, H. Yu and H. Zhao, *Appl. Surf. Sci.*, 2017, **396**, 986–993.
86 R. Nie, X. Peng, H. Zhang, X. Yu, X. Lu, D. Zhou and Q. Xia, *Catal. Sci. Technol.*, 2017, **7**, 627–634.
87 P. Zhang, Y. Gong, H. Li, Z. Chen and Y. Wang, *Nat. Commun.*, 2013, **4**, 1593.
88 D. He, W. Zhao, P. Li, Z. Liu, H. Wu, L. Liu, K. Han, L. Liu, Q. Wan, F. K. Butt and X. Qu, *Appl. Surf. Sci.*, 2019, **465**, 303–312.
89 Y.-F. Lu, S.-T. Lo, J.-C. Lin, W. Zhang, J.-Y. Lu, F.-H. Liu, C.-M. Tseng, Y.-H. Lee, C.-T. Liang and L.-J. Li, *ACS Nano*, 2013, **7**, 6522–6532.
90 L. Qu, Y. Liu, J.-B. Baek and L. Dai, *ACS Nano*, 2010, **4**, 1321–1326.
91 V. B. Parambhath, R. Nagar and S. Ramaprabhu, *Langmuir*, 2012, **28**, 7826–7833.
92 G. Tuci, C. Zafferoni, A. Rossin, L. Luconi, A. Milella, M. Ceppatelli, M. Innocenti, Y. F. Liu, C. Pham-Huu and G. Giambastiani, *Catal. Sci. Technol.*, 2016, **6**, 6226–6236.
93 K. N. Wood, R. O'Hayre and S. Pylypenko, *Energy Environ. Sci.*, 2014, **7**, 1212–1249.
94 Z.-W. Liu, F. Peng, H.-J. Wang, H. Yu, W.-X. Zheng and J. Yang, *Angew. Chem., Int. Ed.*, 2011, **50**, 3257–3261.
95 N. Li, Z. Wang, K. Zhao, Z. Shi, Z. Gu and S. Xu, *Carbon*, 2010, **48**, 255–259.
96 Y. Wang, Y. Shao, D. W. Matson, J. Li and Y. Lin, *ACS Nano*, 2010, **4**, 1790–1798.
97 B. M. Matsagar, C. Van Nguyen, M. S. A. Hossain, M. T. Islam, Y. Yamauchi, P. L. Dhepe and K. C. W. Wu, *Sustainable Energy Fuels*, 2018, **2**, 2148–2153.
98 X. Duan, D. Li, H. Zhang, J. Ma and W. Zheng, *Chem. – Eur. J.*, 2013, **19**, 7231–7242.
99 J. A. Lacey, J. E. Aston, T. L. Westover, R. S. Cherry and D. N. Thompson, *Fuel*, 2015, **160**, 265–273.
100 J. L. Figueiredo, *J. Mater. Chem. A*, 2013, **1**, 9351–9364.
101 L. He, F. Weniger, H. Neumann and M. Beller, *Angew. Chem., Int. Ed.*, 2016, **55**, 12582–12594.
102 H. Yang, R. Nie, W. Xia, X. Yu, D. Jin, X. Lu, D. Zhou and Q. Xia, *Green Chem.*, 2017, **19**, 5714–5722.
103 J. Zhang, Z. Xia and L. Dai, *Sci. Adv.*, 2015, **1**, e1500564.
104 Y.-T. Liao, J. E. Chen, Y. Isida, T. Yonezawa, W.-C. Chang, S. M. Alshehri, Y. Yamauchi and K. C. W. Wu, *ChemCatChem*, 2016, **8**, 502–509.
105 B. Chen, C. Zhang, L. Niu, X. Shi, H. Zhang, X. Lan and G. Bai, *Chem. – Eur. J.*, 2018, **24**, 3481–3487.
106 C. V. Nguyen, Y.-T. Liao, T.-C. Kang, J. E. Chen, T. Yoshikawa, Y. Nakasaka, T. Masuda and K. C. W. Wu, *Green Chem.*, 2016, **18**, 5957–5961.
107 N.-L. Liu, S. Dutta, R. R. Salunkhe, T. Ahamad, S. M. Alshehri, Y. Yamauchi, C.-H. Hou and K. C. W. Wu, *Sci. Rep.*, 2016, **6**, 28847.
108 Y. Gao, G. Hu, J. Zhong, Z. Shi, Y. Zhu, D. S. Su, J. Wang, X. Bao and D. Ma, *Angew. Chem., Int. Ed.*, 2013, **52**, 2109–2113.
109 J. Long, X. Xie, J. Xu, Q. Gu, L. Chen and X. Wang, *ACS Catal.*, 2012, **2**, 622–631.
110 S. Liao, Y. Chi, H. Yu, H. Wang and F. Peng, *ChemCatChem*, 2014, **6**, 555–560.
111 S.-I. Fujita, K. Yamada, A. Katagiri, H. Watanabe, H. Yoshida and M. Arai, *Appl. Catal., A*, 2014, **488**, 171–175.
112 C. Van Nguyen, J. R. Boo, C.-H. Liu, T. Ahamad, S. M. Alshehri, B. M. Matsagar and K. C. W. Wu, *Catal. Sci. Technol.*, 2020, **10**, 1498–1506.
113 Y. Ren, Z. Yuan, K. Lv, J. Sun, Z. Zhang and Q. Chi, *Green Chem.*, 2018, **20**, 4946–4956.
114 Y. Lin, G.-P. Lu, X. Zhao, X. Cao, L. Yang, B. Zhou, Q. Zhong and Z. Chen, *Mol. Catal.*, 2020, **482**, 110695.
115 L. Xu, Z. Han, Y. Zhang and Y. Fu, *RSC Adv.*, 2016, **6**, 108217–108228.
116 Z. He, B. Dong, W. Wang, G. Yang, Y. Cao, H. Wang, Y. Yang, Q. Wang, F. Peng and H. Yu, *ACS Catal.*, 2019, **9**, 2893–2901.
117 A. Nieto-Márquez, D. Toledano, P. Sánchez, A. Romero and J. L. Valverde, *J. Catal.*, 2010, **269**, 242–251.
118 M. Li, F. Xu, H. Li and Y. Wang, *Catal. Sci. Technol.*, 2016, **6**, 3670–3693.

119 X. Xu, M. Tang, M. Li, H. Li and Y. Wang, *ACS Catal.*, 2014, **4**, 3132–3135.
120 N. Daems, X. Sheng, I. F. J. Vankelecom and P. P. Pescarmona, *J. Mater. Chem. A*, 2014, **2**, 4085–4110.
121 Q. Wang and D. Astruc, *Chem. Rev.*, 2020, **120**, 1438–1511.
122 A. Shah, A. Zahid, H. Subhan, A. Munir, F. J. Iftikhar and M. Akbar, *Sustainable Energy Fuels*, 2018, **2**, 1398–1429.
123 A. Sarapuu, E. Kibena-Põldsepp, M. Borghei and K. Tammeveski, *J. Mater. Chem. A*, 2018, **6**, 776–804.
124 J. P. Paraknowitsch and A. Thomas, *Energy Environ. Sci.*, 2013, **6**, 2839–2855.
125 Z. Yang, H. Nie, X. a. Chen, X. Chen and S. Huang, *J. Power Sources*, 2013, **236**, 238–249.
126 W. Y. Wong, W. R. W. Daud, A. B. Mohamad, A. A. H. Kadhum, K. S. Loh and E. H. Majlan, *Int. J. Hydrogen Energy*, 2013, **38**, 9370–9386.
127 Y. Shao, J. Sui, G. Yin and Y. Gao, *Appl. Catal., B*, 2008, **79**, 89–99.
128 T. Sharifi, G. Hu, X. Jia and T. Wågberg, *ACS Nano*, 2012, **6**, 8904–8912.
129 Y. Sun, S. Li, Z. P. Jovanov, D. Bernsmeier, H. Wang, B. Paul, X. Wang, S. Kühl and P. Strasser, *ChemSusChem*, 2018, **11**, 3388–3395.
130 D. Higgins, Z. Chen and Z. Chen, *Electrochim. Acta*, 2011, **56**, 1570–1575.
131 H. Jiang, J. Gu, X. Zheng, M. Liu, X. Qiu, L. Wang, W. Li, Z. Chen, X. Ji and J. Li, *Energy Environ. Sci.*, 2019, **12**, 322–333.
132 X. Yang, K. Li, D. Cheng, W.-L. Pang, J. Lv, X. Chen, H.-Y. Zang, X.-L. Wu, H.-Q. Tan, Y.-H. Wang and Y.-G. Li, *J. Mater. Chem. A*, 2018, **6**, 7762–7769.
133 H.-W. Liang, W. Wei, Z.-S. Wu, X. Feng and K. Müllen, *J. Am. Chem. Soc.*, 2013, **135**, 16002–16005.
134 C.-Z. Guo, W.-L. Liao and C.-G. Chen, *J. Power Sources*, 2014, **269**, 841–847.
135 M. Zhang, Y. Song, H. Tao, C. Yan, J. Masa, Y. Liu, X. Shi, S. Liu, X. Zhang and Z. Sun, *Sustainable Energy Fuels*, 2018, **2**, 1820–1827.
136 Y. Jiao, Y. Zheng, M. Jaroniec and S. Z. Qiao, *J. Am. Chem. Soc.*, 2014, **136**, 4394–4403.
137 W. Ai, Z. Luo, J. Jiang, J. Zhu, Z. Du, Z. Fan, L. Xie, H. Zhang, W. Huang and T. Yu, *Adv. Mater.*, 2014, **26**, 6186–6192.
138 T. Liu, Y.-F. Guo, Y.-M. Yan, F. Wang, C. Deng, D. Rooney and K.-N. Sun, *Carbon*, 2016, **106**, 84–92.
139 T. Akhter, M. M. Islam, S. N. Faisal, E. Haque, A. I. Minett, H. K. Liu, K. Konstantinov and S. X. Dou, *ACS Appl. Mater. Interfaces*, 2016, **8**, 2078–2087.
140 Z. Sun, J. Masa, P. Weide, S. M. Fairclough, A. W. Robertson, P. Ebbinghaus, J. H. Warner, S. C. E. Tsang, M. Muhler and W. Schuhmann, *J. Mater. Chem. A*, 2015, **3**, 15444–15450.
141 S. Yang, L. Zhi, K. Tang, X. Feng, J. Maier and K. Müllen, *Adv. Funct. Mater.*, 2012, **22**, 3634–3640.
142 K. Parvez, S. Yang, Y. Hernandez, A. Winter, A. Turchanin, X. Feng and K. Müllen, *ACS Nano*, 2012, **6**, 9541–9550.
143 E. Haque, S. Sarkar, M. Hassan, M. S. Hossain, A. I. Minett, S. X. Dou and V. G. Gomes, *J. Power Sources*, 2016, **328**, 472–481.
144 L. Lai, J. R. Potts, D. Zhan, L. Wang, C. K. Poh, C. Tang, H. Gong, Z. Shen, J. Lin and R. S. Ruoff, *Energy Environ. Sci.*, 2012, **5**, 7936–7942.
145 A. Zhao, J. Masa, W. Schuhmann and W. Xia, *J. Phys. Chem. C*, 2013, **117**, 24283–24291.
146 W. He, C. Jiang, J. Wang and L. Lu, *Angew. Chem., Int. Ed.*, 2014, **53**, 9503–9507.
147 D. Gu, R. Ma, Y. Zhou, F. Wang, K. Yan, Q. Liu and J. Wang, *ACS Sustainable Chem. Eng.*, 2017, **5**, 11105–11116.
148 J. Zhang, L. Qu, G. Shi, J. Liu, J. Chen and L. Dai, *Angew. Chem., Int. Ed.*, 2016, **55**, 2230–2234.
149 L. Tao, Q. Wang, S. Dou, Z. Ma, J. Huo, S. Wang and L. Dai, *Chem. Commun.*, 2016, **52**, 2764–2767.
150 F. Zheng, Y. Yang and Q. Chen, *Nat. Commun.*, 2014, **5**, 5261.
151 X. Wang, Q. Weng, X. Liu, X. Wang, D.-M. Tang, W. Tian, C. Zhang, W. Yi, D. Liu, Y. Bando and D. Golberg, *Nano Lett.*, 2014, **14**, 1164–1171.
152 H. Wang, C. Zhang, Z. Liu, L. Wang, P. Han, H. Xu, K. Zhang, S. Dong, J. Yao and G. Cui, *J. Mater. Chem.*, 2011, **21**, 5430–5434.
153 C. Nethravathi, C. R. Rajamathi, M. Rajamathi, U. K. Gautam, X. Wang, D. Golberg and Y. Bando, *ACS Appl. Mater. Interfaces*, 2013, **5**, 2708–2714.
154 Z.-S. Wu, W. Ren, L. Xu, F. Li and H.-M. Cheng, *ACS Nano*, 2011, **5**, 5463–5471.
155 J. Ou, Y. Zhang, L. Chen, Q. Zhao, Y. Meng, Y. Guo and D. Xiao, *J. Mater. Chem. A*, 2015, **3**, 6534–6541.
156 Y. Cui, H. Wang, X. Xu, Y. Lv, J. Shi, W. Liu, S. Chen and X. Wang, *Sustainable Energy Fuels*, 2018, **2**, 381–391.
157 A. K. Mondal, K. Kretschmer, Y. Zhao, H. Liu, H. Fan and G. Wang, *Microporous Mesoporous Mater.*, 2017, **246**, 72–80.
158 D. Li, H. Chen, G. Liu, M. Wei, L.-X. Ding, S. Wang and H. Wang, *Carbon*, 2015, **94**, 888–894.
159 W. Li, S. Hu, X. Luo, Z. Li, X. Sun, M. Li, F. Liu and Y. Yu, *Adv. Mater.*, 2017, **29**, 1605820.
160 C. Ling and F. Mizuno, *Phys. Chem. Chem. Phys.*, 2014, **16**, 10419–10424.
161 C. Vaalma, D. Buchholz and S. Passerini, *J. Power Sources*, 2017, **364**, 33–40.
162 B. Quan, A. Jin, S.-H. Yu, S. M. Kang, J. Jeong, H. D. Abruña, L. Jin, Y. Piao and Y.-E. Sung, *Adv. Sci.*, 2018, **5**, 1700880.
163 X. Xu, H. Zeng, D. Han, K. Qiao, W. Xing, M. J. Rood and Z. Yan, *ACS Appl. Mater. Interfaces*, 2018, **10**, 37172–37180.
164 X. Xiong, G. Wang, Y. Lin, Y. Wang, X. Ou, F. Zheng, C. Yang, J.-H. Wang and M. Liu, *ACS Nano*, 2016, **10**, 10953–10959.
165 J. Li, X. Li, D. Xiong, Y. Hao, H. Kou, W. Liu, D. Li and Z. Niu, *RSC Adv.*, 2017, **7**, 55060–55066.
166 W.-C. Chang, K.-W. Tseng and H.-Y. Tuan, *Nano Lett.*, 2017, **17**, 1240–1247.
167 Y. Zhai, Y. Dou, D. Zhao, P. F. Fulvio, R. T. Mayes and S. Dai, *Adv. Mater.*, 2011, **23**, 4828–4850.

168 Y. Zhu, M. Chen, Y. Zhang, W. Zhao and C. Wang, *Carbon*, 2018, **140**, 404–412.
169 Z. Ling, Z. Wang, M. Zhang, C. Yu, G. Wang, Y. Dong, S. Liu, Y. Wang and J. Qiu, *Adv. Funct. Mater.*, 2016, **26**, 111–119.
170 R. J. White, M. Antonietti and M.-M. Titirici, *J. Mater. Chem.*, 2009, **19**, 8645–8650.
171 F. Gao, J. Qu, C. Geng, G. Shao and M. Wu, *J. Mater. Chem. A*, 2016, **4**, 7445–7452.
172 J. Qu, S. Lv, X. Peng, S. Tian, J. Wang and F. Gao, *J. Alloys Compd.*, 2016, **671**, 17–23.
173 R. Shao, J. Niu, J. Liang, M. Liu, Z. Zhang, M. Dou, Y. Huang and F. Wang, *ACS Appl. Mater. Interfaces*, 2017, **9**, 42797–42805.
174 Z. Tian, M. Xiang, J. Zhou, L. Hu and J. Cai, *Electrochim. Acta*, 2016, **211**, 225–233.
175 S.-E. Bae, K.-J. Kim, I.-H. Choi and S. Huh, *Carbon*, 2016, **99**, 8–16.
176 C.-Z. Yuan, H.-B. Li, Y.-F. Jiang, K. Liang, S.-J. Zhao, X.-X. Fang, L.-B. Ma, T. Zhao, C. Lin and A.-W. Xu, *J. Mater. Chem. A*, 2019, **7**, 6894–6900.
177 F. Pan, B. Li, W. Deng, Z. Du, Y. Gang, G. Wang and Y. Li, *Appl. Catal., B*, 2019, **252**, 240–249.
178 D. M. Fernandes, A. F. Peixoto and C. Freire, *Dalton Trans.*, 2019, **48**, 13508–13528.
179 P. Yao, Y. Qiu, T. Zhang, P. Su, X. Li and H. Zhang, *ACS Sustainable Chem. Eng.*, 2019, **7**, 5249–5255.
180 A. S. Varela, W. Ju, A. Bagger, P. Franco, J. Rossmeisl and P. Strasser, *ACS Catal.*, 2019, **9**, 7270–7284.
181 N. D. Leonard, S. Wagner, F. Luo, J. Steinberg, W. Ju, N. Weidler, H. Wang, U. I. Kramm and P. Strasser, *ACS Catal.*, 2018, **8**, 1640–1647.
182 X. Zhang, Z. Wu, X. Zhang, L. Li, Y. Li, H. Xu, X. Li, X. Yu, Z. Zhang, Y. Liang and H. Wang, *Nat. Commun.*, 2017, **8**, 14675.
183 J. Shen, R. Kortlever, R. Kas, Y. Y. Birdja, O. Diaz-Morales, Y. Kwon, I. Ledezma-Yanez, K. J. P. Schouten, G. Mul and M. T. M. Koper, *Nat. Commun.*, 2015, **6**, 8177.
184 B. Reuillard, K. H. Ly, T. E. Rosser, M. F. Kuehnel, I. Zebger and E. Reisner, *J. Am. Chem. Soc.*, 2017, **139**, 14425–14435.
185 F. Li, M. Xue, G. P. Knowles, L. Chen, D. R. MacFarlane and J. Zhang, *Electrochim. Acta*, 2017, **245**, 561–568.
186 A. J. Kamphuis, F. Picchioni and P. P. Pescarmona, *Green Chem.*, 2019, **21**, 406–448.
187 P. Wang, Y. Ren, R. Wang, P. Zhang, M. Ding, C. Li, D. Zhao, Z. Qian, Z. Zhang, L. Zhang and L. Yin, *Nat. Commun.*, 2020, **11**, 1576.
188 Y. Xu, C. Zhang, M. Zhou, Q. Fu, C. Zhao, M. Wu and Y. Lei, *Nat. Commun.*, 2018, **9**, 1720.
189 W. Gong, Y. Lin, C. Chen, M. Al-Mamun, H.-S. Lu, G. Wang, H. Zhang and H. Zhao, *Adv. Mater.*, 2019, **31**, 1808341.

